universität wien

MASTER THESIS

title of the thesis
"Towards magnetic levitation in optomechanics"

author
Jonas Schmöle, BSc

in partial fulfillment of the degree
Master of Science (MSc)

Vienna, 2011

Master thesis

Towards magnetic levitation in optomechanics

Jonas Schmöle[*]

May 19, 2011
supervised by Univ.-Prof. Dr. Markus Aspelmeyer

Abstract

High quality mechanical systems are of interest in the field of optomechanics. We discuss if the levitation of mirrors attached to diamagnets trapped in static magnetic fields can provide a feasible route towards high-Q mechanical oscillators at room temperature. We experimentally analyze the mechanical properties of levitated pyrolytic graphite using optical readout. A theoretical model for the mechanical modes, frequencies and damping by air and eddy currents is provided and compared to the experiment.

Zusammenfassung

Mechanische Systeme hoher Güte sind von besonderem Interesse auf dem Gebiet der Optomechanik. Wir diskutieren, ob die Levitation von Spiegeln auf Diamagneten in permanentmagnetischen Fallen einen möglichen Zugang zu mechanischen High-Q-Oszillatoren bei Raumtemperatur eröffnen kann. Wir analysieren experimentell die mechanischen Eigenschaften von levitiertem pyrolytischen Graphit mit einem optischen Ausleseverfahren. Ein theoretisches Modell für die mechanischen Moden, Frequenzen und Verluste durch Luftreibung und Wirbelströme wird beschrieben und mit dem Experiment verglichen.

[*]jonas.schmoele@univie.ac.at

Contents

1. Introduction

Optomechanics [1, 2, 3, 4] is currently receiving considerable interest as being a cross field discipline of quantum optics, solid state physics and nano-/micro-fabrication. The field focuses on the creation and manipulation of nano- and micro-structures with the goal to bring these systems into regimes where the center of mass motion is dominated by quantum laws and hence they behave as macroscopic quantum objects, even though they consist of several billion atoms. More than 75 years after the first thoughts on quantum effects in macroscopic systems, i.e. *Schrödinger's cat* [5], technology in optics- and structure-fabrication has advanced to a point where for the first time one might see *macroscopic quantum mechanics* in the lab.

The field of optomechanics utilizes optical cavities to enhance the interaction of light fields with mechanical structures (*cavity optomechanics*). With this, many interesting effects, such as laser cooling based on radiation pressure [6, 7, 8], can be exploited. While the interaction between the mechanics and the light field needs to be strong, one tries to minimize the coupling between the mechanics and its environment. An oscillating micro-structure will "talk" to its environment through dissipation of energy, leading to decoherence. The rate of dissipation is determined by the *quality factor Q*, the fraction of the stored energy and the energy dissipated per cycle, of the oscillator.

Current systems rely on a rigid suspension between the oscillating structure and its environment. Recently new ideas towards yet unexplored systems in optomechanics were proposed which drop rigid connections in favor of levitated structures. This might be realized by optical levitation of microspheres [9, 10, 11] or mirrors [12]. Even levitation by repulsive casimir forces might be possible [13].

In this thesis we focus on a magnetic levitation approach towards optomechanics at room temperature, which is possible with materials inhabiting strong diamagnetism. Similar systems have been proposed to be used in MEMS accelerometers [14], but have not yet been exploited as high-Q oscillators. We study the main loss mechanisms in such a diamagnetically levitated system by setting up an appropriate experiment and working out a theoretical model to describe the mechanics. Ultimately we want to show if mechanical levitation schemes can be a competitive approach for optomechanics.[1]

---

[1]Since the rate with which a system couples to its environment is independent of its frequency (appendix B.1), high-Q systems are very interesting even if they have (comparably) low frequencies.

An overview over the topic of magnetic levitation and the different possible schemes is provided in section 2. In sections 3 and 4 we describe an experimental setup in order to characterize the mechanical properties of a particular magnetically levitated system and the results we obtained with it. A better understanding of the results from the experiment is achieved with a numerical model of the mechanics (section 5) and an analytical treatment of energy dissipation mechanisms (section 6). We summarize the results in section 7 and give an outlook on possible ways to improve the current geometry and to set up advanced experiments.

2. Magnetic levitation

Typically one envisions the term *magnetic levitation* as a strong permanent magnet floating over a (type II) superconductor in a bath of liquid nitrogen. Another popular image is that of a superconductor sliding almost frictionless on a rail of permanent magnets. However, those schemes rely on the *flux pinning* effect [15] and are only two special cases of a bigger class of static magnetic levitation effects we describe here.[1]

2.1. Earnshaw's theorem

The reason why levitation in general appears quite fascinating to us is that it seems to be unexplainable with most everyday-forces we experience. Mathematically, this is expressed through *Earnshaw's theorem* [16]. It states that with *any* combination of forces obeying a $1/r^2$ law, like

$$\boldsymbol{F}_G = -G\,\frac{m_1\,m_2}{r^2}\,\boldsymbol{e}_r \qquad\qquad \text{gravity,}$$

$$\boldsymbol{F}_E = \frac{1}{4\pi\,\epsilon_0}\,\frac{q_1\,q_2}{r^2}\,\boldsymbol{e}_r \qquad\qquad \text{electrostatic force,}$$

it is not possible to achieve stable levitation. The reason is that stability requires a (local) minimum in the overall potential U, which makes it necessary that the Laplacian of the potential is greater than zero in some finite connected region,

$$\nabla^2 U \overset{!}{>} 0 \quad somewhere.$$

Since $1/r^2$ forces are always related to $1/r$ potentials and

$$\nabla^2 \frac{1}{r} = 0 \quad \forall\, r$$

one sees that stable levitation is not possible with these forces.[2]

---

[1]In this context, *static* means that there is no need for actively modulated time-dependent magnetic fields.

[2]If you start to think about this statement more deeply, you might ask the question why one can achieve stability without active regulation in everyday situations (e.g. a book lying on a shelf, a person standing on the floor), since collision of rigid bodies is mainly due to electrostatic repulsion. The answer is that Earnshaw's theorem is strictly only valid for point-like particles in given potentials and does not account for rigid lattices of particles or continuous distributions.

A similar situation occurs for objects with a magnetic moment $\boldsymbol{m}$ in a magnetic field $\boldsymbol{B}$, where [17]

$$U = -\boldsymbol{m} \cdot \boldsymbol{B}\,.$$

For paramagnets, $\boldsymbol{m}$ is constant and

$$\nabla^2 \boldsymbol{B} = \nabla(\nabla \boldsymbol{B}) - \nabla \times (\nabla \times \boldsymbol{B}) = 0$$

from the Maxwell equations for the static case in absence of charges. Therefore, $\nabla^2 U = 0$ and Earnshaw's theorem does also apply for paramagnets.

2.2. Loopholes in Earnshaw's theorem

It is clear that if one wants to establish magnetic levitation, one has to find a way to work around Earnshaw's theorem. One way to do this is to "allow" periodic motion of the levitated object, e.g. a gyroscope (an object with cylindrical symmetry spinning around its symmetry axis). Such an object would, once it is levitated, not change its orientation or center of mass position due to gyroscopic forces and therefore appear as being effectively static for most practical reasons. The *Levitron* [18] is such a spinning top built around a permanent magnet, which levitates above another permanent magnet (with opposite pole orientation) as long as its spinning fast enough. For a full treatment of the physics involved, see e.g. [19].

Another way to achieve magnetic levitation despite Earnshaw's theorem is to use materials which do not have a fixed magnetic moment $\boldsymbol{m}$, but one which depends on the field $\boldsymbol{B}$ the material is brought into. Those materials are *diamagnets* and *paramagnets*, where

$$\mathrm{d}\boldsymbol{m} = \frac{V}{\mu_0}\chi\,\mathrm{d}\boldsymbol{B} \quad \text{with} \quad \begin{cases} \chi > 0 & \text{for paramagnets,} \\ -1 \le \chi < 0 & \text{for diamagnets.} \end{cases}$$

The work necessary to switch on a magnetic field from 0 to $\boldsymbol{B}$ in presence of a dia- or paramagnetic object is expressed as[3]

$$\mathrm{d}U = -\mathrm{d}\boldsymbol{m} \cdot \boldsymbol{B} \quad \Rightarrow \quad U = -\frac{V}{2\,\mu_0}\chi\boldsymbol{B}^2.$$

Since $\nabla^2 \boldsymbol{B}^2 \ge 0$ (appendix B.2), $\nabla^2 U$ can be positive for $-1 < \chi < 0$ leading to the possibility to achieve magnetic levitation with diamagnets. The phenomenon of diamagnets *repelling* magnetic fields is known as the *Meissner effect* [15]. It is most extreme for a type I superconductor where $\chi = -1$ and no magnetic field lines can penetrate the object.

---

[3]This is only valid for point-like, isotropic objects. The generalized case is treated in section 5.

2.3. Diamagnetic levitation

One can distinguish two types of diamagnetic levitation [20]:

- Levitation of a diamagnet, where one levitates a diamagnetic object in a permanent field (section 2.3.1),

- diamagnetically stabilized levitation, where one levitates a small permanent magnet using a strong permanent magnet and stabilizes the levitation with diamagnets (section 2.3.2).

Both schemes can also be varied by using superconductors (section 2.3.3).

2.3.1. Levitation of a diamagnet

The levitation of a diamagnetic object using a strong magnetic field gained huge popularity not only among physicists in 1997, when the stable levitation of a living frog in a 16 Tesla bitter magnet was demonstrated [21, 20]. As seen above, stable levitation of a point-like diamagnet requires a local minimum in the total magnetic field strength. For the geometry of a solenoid orientated in vertical direction, such a point can be found towards the upper end of the solenoid. If the field is strong enough, even the weak diamagnetism of water inside the frog is enough to achieve stable levitation. For a cylindrical symmetry, it is possible to have an analytical treatment of the situation and to write down stability criteria [21].

One does not necessarily need very strong magnets to achieve levitation of a diamagnet. A "living-room diamagnetic levitation" setup can be bought as toy. It works with comparably weak *rare-earth* magnets (roughly 1 Tesla) but uses the extremely strong diamagnetism of pyrolytic graphite. Eventually we used this kind of setup for the experiment described below.

2.3.2. Diamagnetically stabilized levitation

One can also use diamagnet blocks of bismuth or graphite to stabilize an otherwise unstable levitation of a permanent magnet with a strong lifter magnet (also permanent) [22, 23]. The drawbacks of this elegant scheme are the low frequencies achievable, which are in the regime of 10 Hz and the difficulties in optical addressability, since the diamagnetic blocks need to be close to the permanent magnets from two sides in the oscillation direction. Also, there is no constraint in the geometry which keeps the levitated magnet from rotating around its axis and we could not find reliable information about the smallest pure permanent magnets with strong enough fields that could be manufactured.

2.3.3. Levitation using superconductors

Apart from flux-pinning in type II superconductors, which is an effect of impurities and not desirable for quantum physics [24], one can use superconductors for their property of being perfect diamagnets ($\chi = -1$) [15], making them usable for the schemes proposed above. The advantage is that the occurring forces are larger by several magnitudes and currents are lossless within the superconductors. The disadvantage is that all known superconductors require cryogenic temperatures to reach their superconducting state, which makes the experimental setup more sophisticated and leads to additional challenges. These include the cooling of an object which starts to levitate at a critical temperature and the need for ultra-reflecting mirror coatings to avoid heating through absorption.[4]

---

[4]This problem is less present with standard mechanical oscillators, since they can dissipate heat to their (cooled) environment. However, a levitated structure can only dissipate heat through black body radiation, so the heating of the structure through absorption and the cooling through black body radiation have to balance at a temperature below the critical temperature of the superconductor.

3. Experimental Setup

The goal of the experimental work done was to create a sample using diamagnetic levitation, to have a way to read out its position and orientation and to apply a suitable measurement scheme to determine the mechanical properties.

We chose to levitate a diamagnet as described in section 2.3.2 with the sample described below (section 3.1). The read-out of the sample was done optically by reflection of a collimated beam on a mirror put on the sample (section 3.2). The advantage of an optical readout is that it makes it easy to resolve different degrees of freedom in the motion of the sample. Also, in the context of optomechanics, the optical addressability is obligatory anyway. A vacuum chamber for the sample was designed to see how its properties change with pressure (section 3.3).

Eventually we applied three different measurement schemes to characterize the system, all of them with certain (dis-)advantages (section 3.5).

3.1. The sample

To the author's knowledge, few publications exist that give explicit information on materials that are suitable for diamagnetic levitation, with the only material known to work being *pyrolytic graphite*. Thin sheets of pyrolytic graphite can be levitated on different compositions of strong permanent magnets.

3.1.1. Levitated diamagnet

A commercial piece of pyrolytic graphite was used for levitation. In the direction orthogonal to its internal carbon layers, pyrolytic graphite has the highest diamagnetic susceptibility and by far the highest mass susceptibility (which is important for levitation, since the weight needs to be lifted) at room temperature among all materials known.

The important parameters of the sample we used are summarized in table 3.1. The shape was chosen to be non-square to avoid close eigenfrequencies which are hard to resolve experimentally. For the orientation readout described below, we put a GaAs mirror on the sample using a small drop of adhesive (figure 3.1a).

Pyrolytic graphite is a very inhomogeneous, rough material which is not suitable to create clean, polished surfaces one would need to grow thin mirror layers on it. However, there is an alternative called *highly ordered pyrolytic graphite* which

symbol	description	value
m	weight (incl. mirror)	$61.5\,\text{mg}$
$\boldsymbol{s}$	dimensions	$(6.85, 7.95, 0.3)^T\,\text{mm}$
χ	susceptibility tensor	$\begin{pmatrix} -1.4{\cdot}10^{-5} & & \\ & -1.4{\cdot}10^{-5} & \\ & & -6.1{\cdot}10^{-4} \end{pmatrix}$
I	inertia tensor	$\begin{pmatrix} 3.27{\cdot}10^{-10} & & \\ & 2.43{\cdot}10^{-10} & \\ & & 5.69{\cdot}10^{-10} \end{pmatrix}\,\text{m}^2\,\text{kg}$

Table 3.1.: Parameters for the sample used throughout the experiments: A piece of pyrolytic graphite with a gallium arsenide (GaAs) mirror with slightly smaller dimensions glued to the surface. All values are given in Cartesian coordinates with axes parallel to the sample edges.

was not available for this experiment but does have properties which could make it suitable to create nice micromechanical samples [25]. Both variants of pyrolytic graphite are highly anisotropic, with a distinct axis of strong diamagnetism and weak conductivity.

3.1.2. Array of magnets

We used the most simple configuration of magnets which is known to work and which stabilizes a rectangular shaped sheet of pyrolytic graphite in all degrees of freedom. This is a checkerboard configuration of four strong cube magnets (figure 3.1, table 3.1).
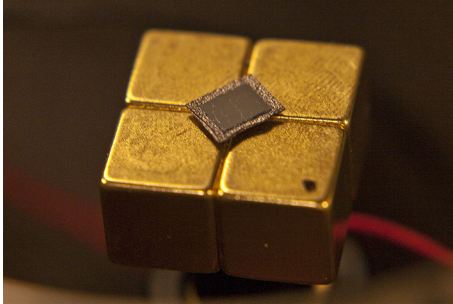
(a) Array of gold-coated magnets with levitated graphite and attached GaAs mirror.
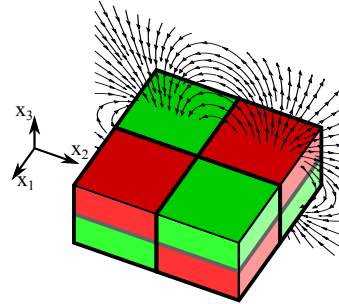
(b) Checkerboard configuration of magnets with a plane through the magnetic field lines.

Figure 3.1.: Magnet array for levitation of graphite. The geometry allows for four stable levitation positions obtained by rotation of the graphite in steps of $90°$ around x_3.

Even though the exact shape of the potential is not obvious (and in fact strongly depends on the individual tensor components χ_{ij} of the levitated diamagnet), it is easy to see that this configuration leads to a diamagnetic potential which is zero along the x_3-axis and increases when going away from it. Remember that diamagnets are repelled by strong field amplitudes $|\boldsymbol{B}|$ and notice that due to the two fold mirror symmetry the magnetic fields of each individual magnets cancel out along the x_3-axis but nowhere else. One finds the strongest amplitude of $\boldsymbol{B}$ at the center of the upper surface of each individual magnet. Adding the homogeneous force of gravity, at one point on the x_3-axis one obtains an effective total potential well for a diamagnet in all six degrees of freedom:

- The translation in x_1- and x_2-direction as well as the according rotations are controlled by the increasing total field amplitude within the diamagnet,

- the rotation about the x_3-axis is covered by the twofold mirror symmetry of the potential,

- the x_3-translation sees a potential minimum where diamagnetic repulsion and gravitational attraction balance.

From this geometry, it is evident that the diamagnet must have a certain minimal size in order to get levitated by the magnets. A point-particle would simply fall along the x_3-axis, since it does not feel any field there. The minimal size depends on the strength of the magnets and the susceptibility χ of the diamagnet.

symbol	description	value
$\boldsymbol{l}$	dimensions	$(12.0, 12.0, 12.0)^T$ mm
B_0	surface field	1.4 T
M_0	magnetization	$866\text{-}995 \cdot 10^3$ A/m

Table 3.2.: Parameters for the array of magnets used throughout most measurements; values taken from specification of manufacturer.

The diagonal equilibrium orientation of the rectangular sheet of graphite is explained by its anisotropy. Because the diamagnetism is much stronger along the axis orthogonal to the plane, the diamagnetic repulsion is mainly determined by B_3^2 instead of $|\boldsymbol{B}|^2$. An isotropic diamagnet would maintain an equilibrium with its edges parallel to those of the magnets. The effect is visualized in figure 3.2.

The magnets in our experiments are NdFeB *rare-earth* magnets [26] with a gold coating (since the material is highly corrosive) and have the properties listed in table 3.2.

The levitation height in this configuration was measured to be $0.5[2]$ mm.

(a) Equipotential surface of B_3^2 (as seen by pyrolytic graphite with strong diamagnetism along x_3).

(b) Equipotential surface of $|\boldsymbol{B}|^2$ (as seen by an isotropic diamagnet with equal diamagnetism in all directions).
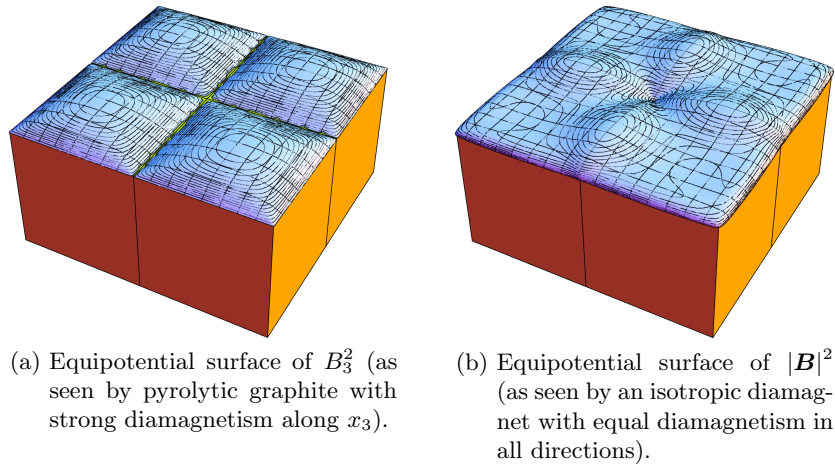
Figure 3.2.: Dependence of equipotential surfaces on the isotropy of the susceptibility tensor.

3.2. Position and orientation readout

The position readout of the sample is implemented using a simple reflection scheme as shown in figure 3.3a, equivalent to a Michelson interferometer. A collimated fiber beam with a wavelength of 1064 nm is split on a beam splitter. One path is reflected at the mirror on the sample, the other path on a fixed mirror. Because of the slight divergence of the beam, the two mirrors are adjusted such that the distance from the beam splitter to the mirrors is about equal. Both beams are reflected and interfere at the output of the beam splitter where they are focused on a quadrant diode. This setup allows for two different readout schemes of the mechanics:

- In the *interferometric scheme* one measures the total intensity at the diodes and therefore observes the interference fringes through the vertical displacement of the sample. If the beam hits the center of the sample, only the translation along x_3 direction is visible.

- In the *displacement scheme* one blocks the path with the fixed mirror. A change of the orientation of the sample leads to a displacement of the spot on the diode.[1] With a quadrant-diode, both tilting directions can be measured independently. Because the quadrant diode is mounted vertically and the beam hitting the sample is adjusted to be not exactly vertical, one can also

---

[1]The lens in the setup was necessary to reduce the displacement of the spot. Without the lens, the spot displacement just by lab noise was multiples of the diode size.
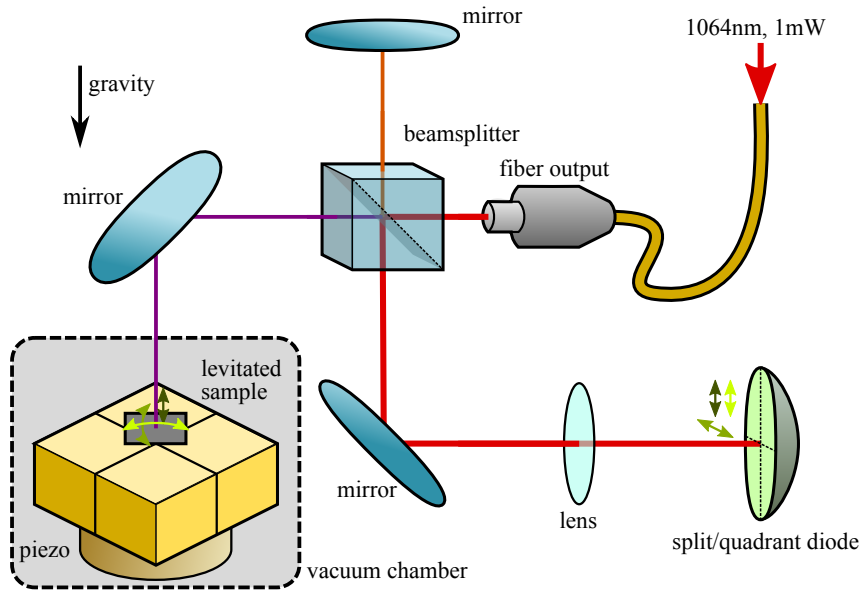
(a) Illustration of the basic readout scheme. The upper vertical beam path can be blocked to perform sample-tilt induced beam displacement measurements. The green arrows indicate the motion of the levitated sample and the according beam displacements visible on the quadrant diode.
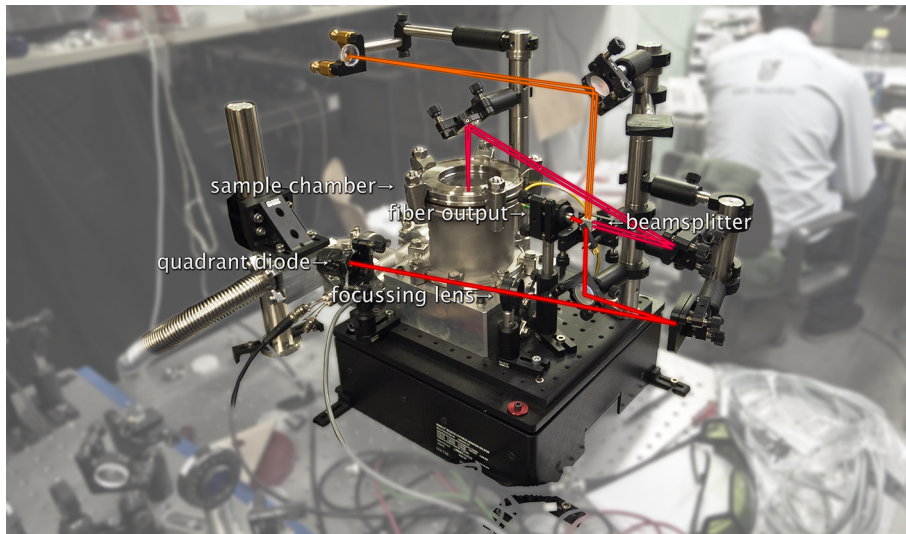
(b) Experimental setup with the vacuum chamber on a low-frequency vibration isolation stage and the vertically mounted interferometer.

Figure 3.3.: Readout scheme and photo of experiment.

11

measure the x_3 displacement - the measurement is just less sensitive than interferometric readout.

It is important to note that displacement in some degrees of freedom will not cause any change of the beam phase or displacement. These are the rotation about the x_3 axis and the translation in x_1 and x_2 direction. If these degrees of freedom correspond to individual modes, i.e. not coupling to *visible* degrees of freedom, there is no direct way of identifying them with this readout scheme.

An actual picture of the setup can be seen in figure 3.3b, including the vacuum chamber described below.

3.3. Vacuum chamber

In order to find the relation between the mechanical quality of the levitated sample and the background pressure, a simple high vacuum chamber was designed (figure 3.4). The requirements were low complexity, fast production time and no need for welding (to exclude sources of leaks). The final design is general-purpose and only uses off-the-shelf components except for the base block. It has two KF25 openings for pumps and gauges and a K100 lid on the top which can either have a window for free-space measurements or a fiber-feedthrough to do fiber interferometry.[2] Because of the versatile design, the chamber can be reused for other experiments which require a quick and simple vacuum solution.
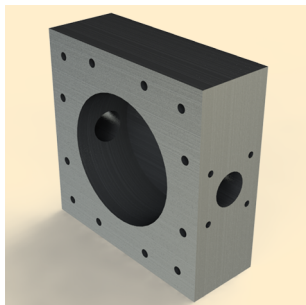
(a) Custom building block of the vacuum chamber (rendered).
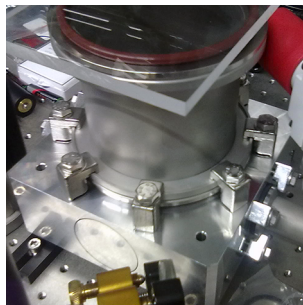
(b) Standard components clamped to the chamber (picture of an early stage of the experiment).
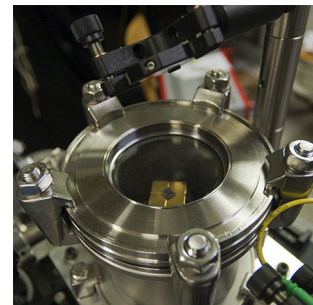
(c) Window on top of the chamber for free space optical access.

Figure 3.4.: Vacuum chamber.

---

[2]Because of huge noise issues with interferometric readout described below, the fiber option was actually never used in this experiment.

Inside the chamber, the suspension magnets are mounted on a piezo which can be driven from outside using a vacuum feedthrough. A gauge is mounted at the chamber for pressure readout. The chamber is evacuated with a Pfeiffer HiCube Eco turbo pump stand.

3.4. Vibration isolation

From the sample weight and the non-rigid suspension, it was reasonable to expect fairly low vibration frequencies (below 100 Hz). Since standard optical tables do not provide good vibration in this range, we mounted the entire setup on an additional *minus k* low-frequency vibration isolation stage. This required mounting the entire optics on a very limited space while maintaining the center of mass above the center of the stage. The stage needs to be locked with four screws before its payload can be modified. For a detailed explanation of the steps which eventually lead to this setup, see appendix B.4.

3.5. Applied methods

In order to minimize systematic errors, we used three different methods to explore the mechanical properties of the system. The required formulas for the driven damped harmonic oscillator, which approximates our system, can be found in appendix A, page 53.

3.5.1. Ringdown

Without external driving, the trajectory of the sample is fully described by the homogeneous solution A.2 to the equations of motion A.1:

$$x(t) = A\,e^{-\zeta\,\omega_0\,t}\,\sin(\sqrt{1-\zeta^2}\,\omega_0\,t + \phi)$$

where A is the amplitude of the ringdown, $\zeta = \frac{1}{2Q}$ is the *damping ratio*, ω_0 is the eigenfrequency of the excited mode and ϕ an arbitrary phase. We utilize this by first driving the system up to a certain amplitude with the frequency of the mode we want to measure. Then the driving is abruptly switched off and the ringdown trajectory is measured and fitted with the equation above. A simplified plot of a single ringdown is shown in figure 3.5a.

A problem with this method is that energy might be transfered into non-visible modes (e.g. rotation about the x_3 axis), which results in a shorter ringdown time and thereby a smaller quality factor. Also, if the correct eigenfrequencies are not exactly known (for example because they change with temperature and other environmental influences), it is almost impossible to drive just one specific mode. Depending on

(a) A single ringdown curve with the envelope.

(b) Cauchy-Lorentz distribution used to fit the individual peaks in both ringdown and noise spectra measurements.
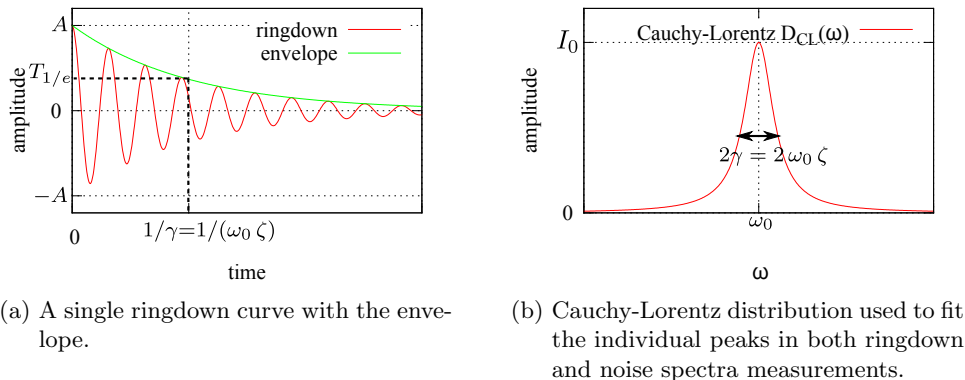
Figure 3.5.: Illustrations of typical Cauchy-Lorentz and ringdown curves.

the frequency separation, the observed oscillation will always be a superposition of several ringdowns.

3.5.2. Lock-in amplification

With the piezo mounted under the magnets, one can indirectly drive the sample. This is used for lock-in measurements as described in appendix A.3. The squared amplitude of the lock-in signal is a *relativistic Breit-Wigner function* and can be approximated with a Cauchy-Lorentz distribution (appendix A.7):

$$|\mathcal{F}(x)(\omega)|^2 = \frac{(F_0/m)^2}{\left(\omega_0^2 - \omega^2\right)^2 + (2\,\zeta\,\omega_0\,\omega)^2} \approx \left(\frac{F_0/m}{2\,\omega_0\,\zeta}\right)^2 \frac{(\zeta\,\omega_0)^2}{(\omega - \omega_0)^2 - (\zeta\,\omega_0)^2}, \quad (3.1)$$

with the damping ratio $\zeta = \frac{1}{2Q}$ and the eigenfrequency ω_0 as above.[3] F_0/m is the driving amplitude divided by the sample mass. The term $\zeta\,\omega_0 =: \gamma$ corresponds to the half width of the peak at the half height of its maximum amplitude (*HWHM*, figure 3.5b).

A disadvantage of this method is that for every measured frequency, one needs to wait for the system to reach the steady-state before one can perform the actual lock-in integration. If the system has a ringdown time of a second, one needs to wait several seconds before being able to measure at each point. For a high-resolution scan over a broad frequency range, a lock-in scan can take several hours, over which the properties of the system might change e.g. due to temperature drifts. The advantage of this method are the very nice and smooth system response curves one gets from it.

---

[3]For ζ it does not matter if one measures ω in radian or not, since the factor of 2π gets absorbed by γ depending on the definition.

3.5.3. Noise spectra

The sample picks up random noise from the lab (e.g. people walking around, air conditioning) which we approximate as being white in the relevant frequency range. We do not apply any direct driving and just observe the systems response to the environment. As described in appendix A.1, one expects that a Fourier transform of a time trace is of relativistic Breit-Wigner form (3.1) very similar to the lock-in signal.

When recording a time trace of low-frequency systems, it is important to trace over a sufficiently long interval. For example, a quality factor $Q = 200$ at a frequency of $20\,\mathrm{Hz}$ corresponds to $\gamma = 0.31\,\mathrm{Hz}$. To resolve this peak, one needs at least 3.2 seconds of data, corresponding to a measurement bandwidth of $0.31\,\mathrm{Hz}$. To resolve $Q = 10000$, the measurement has to run for almost 3 minutes.

Besides the need to record long time traces, the noise spectrum method has another disadvantage when used for a low-frequency system. Any noise from the environment which is not white will show up in the spectrum, usually resulting in sharp peaks with unknown origin.

4. Measurements and results

4.1. Noise spectra of the levitated diamagnet

We estimated the frequency and the mechanical quality by "driving" it with white noise from the lab and fitting a Cauchy–Lorentz distribution (figure 3.5b, see appendix A.4, equation (A.7) for detailed explanation)

$$D_{CL}(\omega) = I_0 \frac{\gamma^2}{(\omega - \omega_0)^2 - \gamma^2}, \qquad (4.1)$$

where I_0 is an arbitrary amplitude, for each individual peak we see in the spectrum obtained by Fourier transformation of a sufficiently long time trace. A spectrum at atmospheric pressure can be seen in figure 4.1a. One can distinguish a number of peaks and noise. Reasonable assumptions for mechanical modes are the peaks at 5 Hz and 20 Hz (see below).
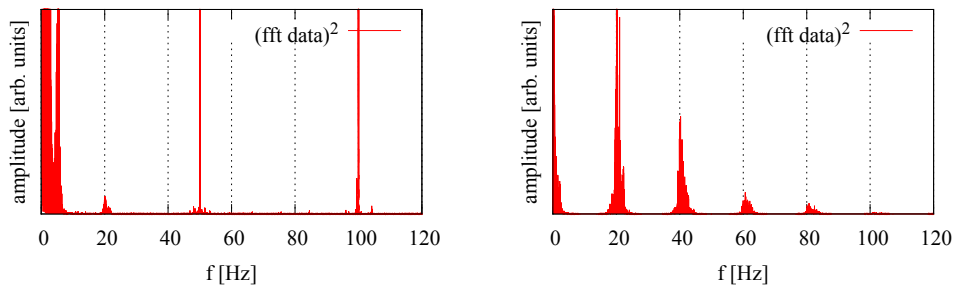
(a) Measurement with intact low-frequency vibration isolation stage. A huge peak at 5 Hz as well as a weaker peak at 20 Hz are visible. Very high Q peaks at 50 Hz and 100 Hz indicate interference from electronics and are most likely not mechanical, since they do not show up on other recording devices.

(b) The same spectrum on a broken isolation stage (see below). The 20 Hz peak becomes so dominant that it suppresses all other peaks. Multiple orders show up.

Figure 4.1.: Typical fourier spectra from interferometric measurements.

The dependence of the quality factor on pressure was determined from the width of the spectra peaks at different pressures. Before each measurement, the valve

at the chamber was closed. The pump was shut down while slowly being flooded to avoid damage and then disconnected. The minus k stage was released from being locked and the beam was realigned. Since the pump must not be connected during the measurement (appendix B.4), we could not reach very low pressures with the HV components. The values at the lower end of the reachable pressure range (roughly 10^{-3} mbar) were taken while the pressure in the chamber was rapidly increasing. Because these measurements were performed just at the border from molecular damping to viscous damping (section 6.1), values in the lower pressure range have to be taken with caution. Unfortunately the vibration isolation stage broke just before the first measurement of the series, which we did not realize until the entire data was collected.

Interferometric measurements and tilt measurements were performed at the same time. In the spectra of the time traces one can only identify one mode at 20 Hz with several higher orders. A typical spectrum is shown in figure 4.1b.

Both interferometric and tilt displacement data show multiple-frequency peaks of the same mode at 20 Hz. For the interferometry data, where the sum of all quadrants was recorded, the higher orders show up because the motion of the sample spans several half-wavelengths of the light. The same holds for the tilt measurement since the overlap of the displaced beam with the undisplaced reference beam causes fringes which shift with a multiple rate of the oscillation frequency.[1]
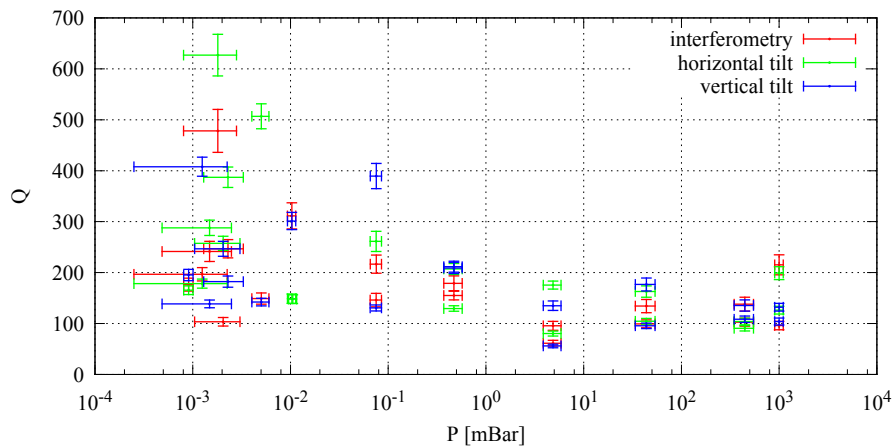
Figure 4.2.: Q versus P for the 20 Hz mode from noise spectra.

The resulting plot of quality factor versus pressure for the 20 Hz mode is shown in figure 4.2. Note that the horizontal axis has a logarithmic scale while the vertical

---

[1]One should investigate if it is possible that the value of Q obtained from fitting just the first of multiple peaks changes compared to a fit where one mathematically deducts the multiple peaks an creates a "clean" spectrum before fitting.

axis is scaled linearly. There seems to be some increase of Q below $1\,\text{mbar}$, but one cannot estimate the shape (logarithmic, linear or exponential). As explained in section 6.1, in the regime below $10^{-2}\,\text{mbar}$ we would expect $Q \propto 1/p$ if air damping was the only damping mechanism.

With the low-frequency vibration isolation stage broken we dropped the interferometric measurements and focused on the tilt displacement scheme. The noise issues (one dominant mode having a particularly strong response to the environmental noise and suppressing all other peaks in the spectrum) in the noise spectra measurements make the data unreliable and suggest that a driven readout scheme is preferable.

4.2. Lock-in amplification scans of the levitated diamagnet

We performed several lock-in scans using different modifications for the sample in order to characterize its properties. The peaks were fitted with the same Cauchy-Lorentz distribution (4.1) as seen before.

During these measurements, only a split diode was available (instead of a quadrant diode)[2]. In order to still be able to resolve both beam displacement degrees of freedom, the whole sample (magnets and levitated graphite) was rotated by 90° for some of the measurements. Therefore we divide the data into *landscape* and *portrait* data. As shown in figure 4.3, in the landscape data the split diode separation line maps onto the (x_1, x_2) axis and makes tilts of the sample around this axis visible, which corresponds to the short axis of the sample. In the portrait data, the separation line maps on the $(x_1, -x_2)$ direction making tilts around the long axis of the sample visible.

Since the sharpness of the piezo driving frequency peak is crucial in the lock-in scheme, we checked it independently without the sample (appendix B.3). The values listed in each following respective table were taken in close succession in the same measurement run.

4.2.1. Frequency scan at atmospheric pressure of the levitated diamagnet

A basic scan where the driving frequency was scanned over a broad range can be seen in figure 4.4. The most dominant peaks are located at approximately 16 and $20\,\text{Hz}$. At higher frequencies, nothing significant happens except for one peak at approximately $60\,\text{Hz}$ which is weaker by roughly one order of magnitude.

---

[2]A split diode consists of two individual diodes. In contrast to a quadrant diode, it can resolve just one direction of beam spot displacement
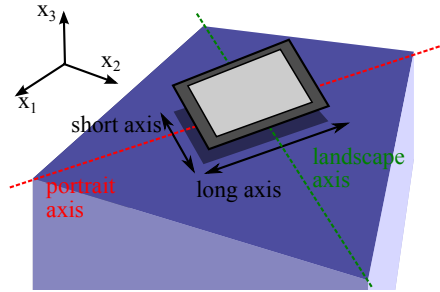
Figure 4.3.: Split axis of the split diode mapped on the sample. In the experiment, not the split diode but the sample itself was rotated. Since the face of the split diode was vertical with the split axis horizontal dividing it in an upper and a lower diode, the x_3 motion was visible in both orientations of the sample.
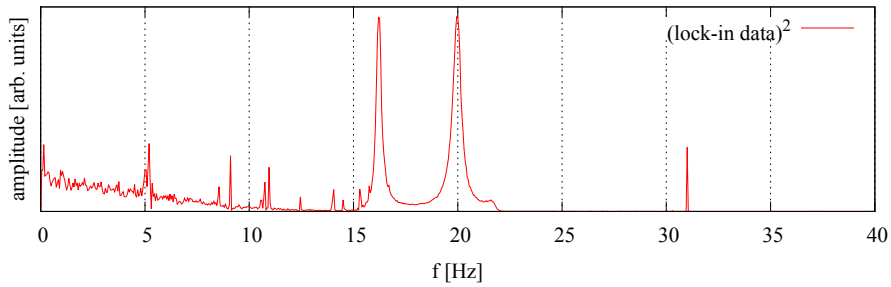
(a) Lock-in spectrum from 0 to 40 Hz.
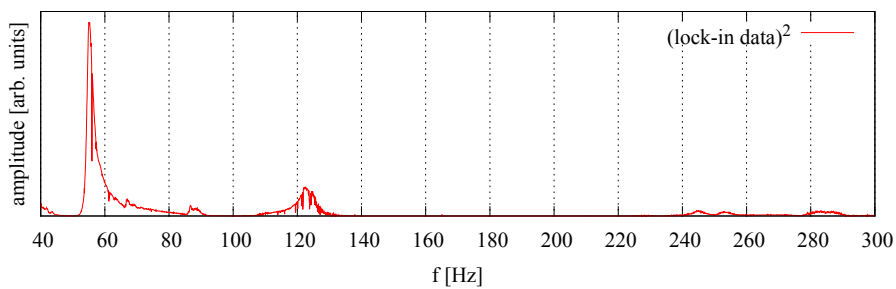
(b) Lock-in spectrum from 40 to 300 Hz; amplitude multiplied by 10.

Figure 4.4.: *Landscape* lock-in scan of the sample at atmospheric pressure.

4.2.2. Identification of mechanical oscillation modes and their quality factors

We focus on the three peaks which were most significant in most scans. They are located at approximately 16.2 Hz, 20.0 Hz and 21.7 Hz (figure 4.5).
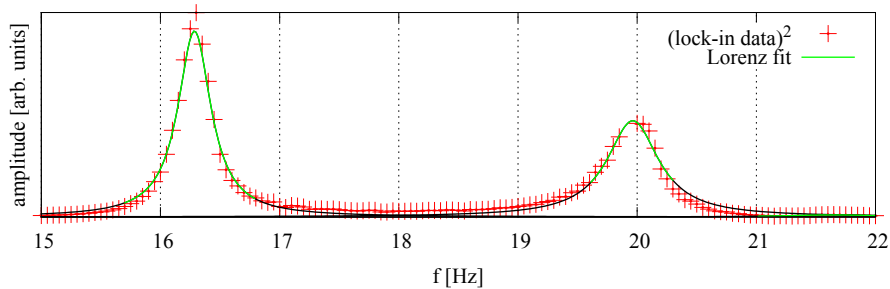
(a) Lock-in spectrum in *landscape* position.
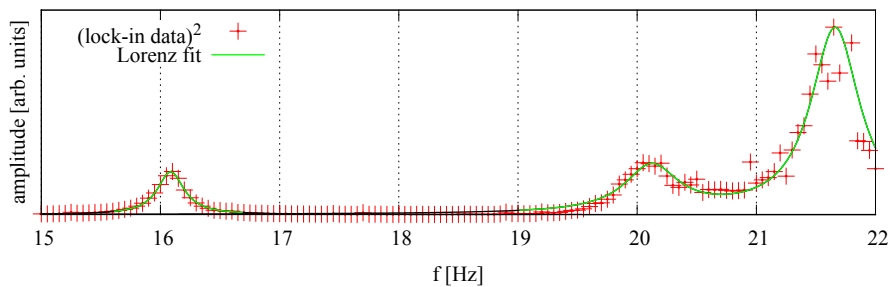
(b) Lock-in spectrum in *portrait* position.

Figure 4.5.: Lock-in scan of the sample in landscape and portrait position with Cauchy-Lorentz fits. The frequency shifts of the visible modes indicate that the reproducibility of the measured frequencies is given to a about 0.5 Hz, even though the fit errors (table 4.1) suggest much smaller errors.

One can see that the 21.7 Hz peak is almost invisible in the landscape orientation but clearly stands out in portrait orientation. For the 16.2 Hz peak, it is the other way around. The 20.0 Hz peak is visible in both orientations. From this we conclude that 20.0 Hz corresponds to the vertical translation (since this motion should be visible on the split diode in both orientations), 16.2 Hz corresponds to a tilting mode around the (x_1, x_2) axis and 21.7 Hz to a tilting mode around the $(x_1, -x_2)$ axis (figure 4.6).

From fitting Cauchy-Lorenz distributions to the squared response curve at atmospheric pressure (figure 4.5), we obtain the quality factors listed in table 4.1.

orientation	f [Hz]	Q
landscape	16.28[1]	48.3[17]
	19.96[1]	37.8[26]
portrait	16.09[1]	59.1[10]
	20.12[7]	36[11]
	21.66[2]	43.2[39]

Table 4.1.: Q at atmospheric pressure from lock-in measurements.

(a) 16.2 Hz   (b) 20.0 Hz   (c) 21.7 Hz
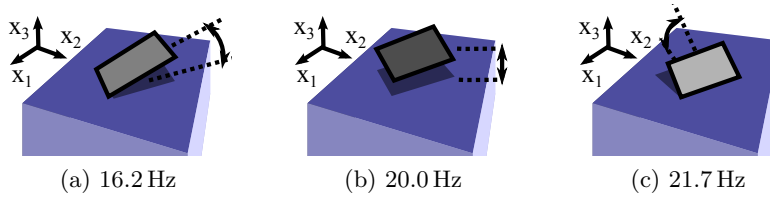
Figure 4.6.: Inferred mechanical oscillation modes from the visible frequencies in figure 4.5. The first mode was only visible when the sample and magnets were rotated such that the division of the split diode corresponds to the (x_1, x_2) axis. For the third mode, the division had to be along $(x_1, -x_2)$. The second mode displayed was visible for both orientations.

4.2.3. Deviations between equilibrium positions

In the previously described measurements, we checked just one of the four possible equilibrium positions obtainable by rotation of the graphite around the x_3 axis. Due to impurities of the graphite amplifying slight deviations of the magnetic field, the four positions might not be degenerate. We checked this by leaving the orientation of the graphite in the setup constant while rotating the permanent magnets to all four positions which allow stable levitation. The data can be seen in table 4.2.

Rotation [°]	f [Hz]	Q
0	16.44[1]	54.0[17]
90	16.93[1]	56.7[13]
180	16.59[1]	51.6[20]
270	17.02[1]	60.1[23]

Table 4.2.: Lock-in scan of the sample in the four stable levitation positions. *Rotation* refers to the relative rotation of the permanent magnets against the standard position used in all other measurements.

It is clearly visible that the frequency of the mode is different for the four orientations, which could be caused by different total magnetizations of the four permanent magnets or a magnetization which is not exactly directed along x_3. Regarding the piece of pyrolytic graphite used throughout the experiments it is no suprise to see such effects, since it does not even *look* homogeneous by visual inspection.

4.2.4. Measured mechanical dependence on the driving amplitude

In the same fashion as in the section above we checked if the amplitude of the driving has an influence on the broadening of the peaks, which might be caused through deviations of the potentials from being harmonic. This is probably *not* the case as you can see from table 4.3. The measured frequencies and quality factors are within the typical fluctuations between measurements.

driving power [V]	f [Hz]	Q
0.25	16.47[2]	54.8[10]
0.5	16.47[2]	55.8[10]
0.75	16.47[2]	58.9[11]
1.0	16.47[2]	57.5[9]

Table 4.3.: Change of mechanical properties with different driving powers from lock-in.

4.2.5. Measured mechanical dependence on pressure

With the modes of the system identified and possible sources of errors excluded, we checked if the mechanical quality of the system increases when going to low pressures. When these measurements were performed, we did not have the possibility to regulate the pressure in the system to certain values. Therefore the measurement was performed at the lowest pressure which could be maintained while the pump was disconnected (otherwise it just caused too much noise), which was about 10^{-2} mbar. In a scan from 14 Hz to 23 Hz in landscape orientation, we got the results listed in table 4.4.

P [mBar]	f_1 [Hz]	Q_1	f_2 [Hz]	Q_2
10^3	16.21[1]	57.6[17]	19.96[1]	41.4[8]
10^{-2}	16.19[1]	61.3[7]	19.93[1]	42.0[3]

Table 4.4.: Change of mechanical quality with decreased pressure from lock-in scans.

Unexpectedly, the measured quality factor does not significantly increase with the

pressure being lowered by five orders of magnitude. This could either mean that there is another dominant loss mechanism already at atmospheric pressure, or that there is a systematic error in the lock-in measurements leading to peak-broadening. To check this, we re-checked the Q versus P dependence in another, independent scheme, which is described in section 4.3.

4.2.6. Measured mechanical dependence on the sample weight

We checked how the frequencies of the modes depend on the mass of the sample by putting additional masses of paper on it, shown in figures 4.7a, 4.7b. The results from the lock-in scan are shown in table 4.5.

total weight [mg]	f_1 [Hz]	Q_1	f_2 [Hz]	Q_2	f_3 [Hz]	Q_3
61.5[1]	16.26[1]	49.6[14]	19.93[2]	41.5[15]	21.48[3]	45.1[58]
64.4[1]	16.05[1]	52.3[9]	19.98[2]	38.0[18]		
67.0[1]	15.74[1]	44.8[8]	20.11[2]	35.9[20]	21.16[2]	47.8[25]

Table 4.5.: Change of mechanical properties with different sample weights derived from lock-in measurements.

Naively one would have expected that the ratio of squared frequencies corresponds to the inverse ratio of total masses, which is the case for the harmonic oscillator (appendix A) as long as the potential does not change. However, adding mass changes the levitation height of the sample and therefore also changes the gradient of the potential around the equilibrium position. This means that we cannot deduce that the 20 Hz peak is not of mechanical nature just because its frequency does not change when adding mass, which we further investigate in section 5.6.3.

(a) Weight 1 (2.9 mg)   (b) Weight 2 (2.6 mg)   (c) Aluminum foil
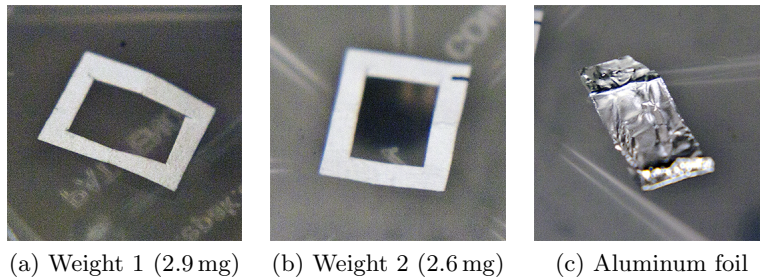
Figure 4.7.: Pieces of paper and aluminium put on the sample to see weight- and damping dependencies.

4.2.7. Measured mechanical dependence on eddy currents

In order to examine the influence of eddy currents, a small piece of aluminum foil was put on the sample (figure 4.7c). It has a mass of $1.6\,\text{mg}$ and dimensions as listed in table 4.6. This significantly broadens the peaks (figure 4.8) and results in a decreased mechanical quality (table 4.7).

symbol	description	value
$\boldsymbol{s}$	dimensions	$(5.0, 8.2, 0.015)^T \,\text{mm}$
m	weight	$1.6\,\text{mg}$
σ	conductivity	$1/\left(40 \cdot 10^{-9}\,\Omega\,\text{m}\right)\,\boldsymbol{1}$

Table 4.6.: Parameters of the aluminum sample used to induce eddy current damping.
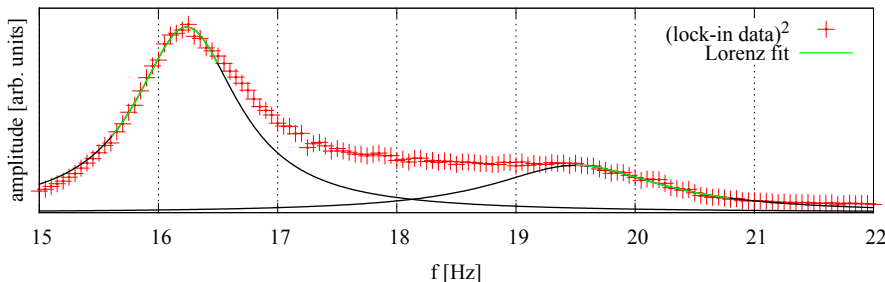
Figure 4.8.: Lock-in scan of the sample with added foil.

sample modification	$f_1\,[\text{Hz}]$	Q_1	$f_2\,[\text{Hz}]$	Q_2	$f_3\,[\text{Hz}]$	Q_3
original	16.29[1]	53.2[8]	19.97[2]	46.1[31]	21.48[3]	45.1[58]
with foil	16.24[1]	15.4[4]	19.50[5]	11.3[6]	21.38[6]	13.8[13]
just foil		21.7[8]		15.0[11]		19.9[29]

Table 4.7.: Change of mechanical properties with induced eddy currents derived from lock-in measurements.

The value given for *just foil* is quality factor corresponding to the damping ratio from just the aluminum foil. We call this a *limiting Q* since without other damping mechanisms, this would be the maximum value of Q achievable. Using (A.4), it is obtained by

$$\frac{1}{Q_{\text{just foil}}} = \frac{1}{Q_{\text{with foil}}} - \frac{1}{Q_{\text{original}}}.$$

These results qualitatively prove that there indeed is a damping mechanism induced through eddy currents generated by the moving graphite in the magnetic field.

4.2.8. Measured mechanical dependence on the size of the magnets

We substituted the gold-coated permanent magnets ($1.4\,\text{T}$) with nickel-coated cube magnets with a slightly weaker surface field of $1.3\,\text{T}$, about the same magnetization ($900 \cdot 10^3\,\text{A/m}$) and a side length of $10\,\text{mm}$. The results are listed in table 4.8.

magnets	f_1 [Hz]	Q_1	f_2 [Hz]	Q_2	f_3 [Hz]	Q_3
gold, $12\,\text{mm}$	16.59[2]	50.5[52]	20.07[2]	42.3[37]	21.56[2]	49.3[53]
nickel, $10\,\text{mm}$	17.42[1]	49.9[19]	20.52[4]	40.53[96]	21.48[2]	41.2[30]

Table 4.8.: Change of mechanical properties with smaller permanent magnets derived from lock-in measurements.

While the frequency of the first mode goes up and the quality factor does not change, the frequency of the third peak is unaffected but the quality factor increased. The second mode appears to be completely unaffected. This could be caused by the stronger gradient in the magnetic field created by the smaller permanent magnets, but there is no obvious interpretation of this behavior. Also, the differences in the frequencies between the two samples almost lie in the range we saw from just changing the orientation of the sample on the magnets (section 4.2.3), so one cannot see in which way the smaller magnets affect the sample modes and frequencies.

4.3. Ringdown curves of the levitated diamagnet

In order the have a third, independent scheme to determine the frequencies and mechanical qualities of the system, we performed ringdown measurements. For these measurements, a quadrant diode was available again. The driving was performed for 30 sinusoidal periods with *silent* intervals of 2 to 3 seconds, depending on the driving frequency. During the silent intervals, ringdown curves were recorded. We averaged the ringdown curves over 15-30 cycles. This is legitimate since after a few transient cycles, the phase of the oscillator is reproduced every time the driving is shut off and therefore, without too much influence from the environment, the ringdown curve should be the same in each cycle. We fitted the curves using a *double-ringdown*

$$x(t) = o + A_1\,e^{-\gamma_1 t}\cos\left(\omega_{01}\,t + \phi_1\right) + A_2\,e^{-\gamma_2 t}\cos\left(\omega_{02}\,t + \phi_2\right) \qquad (4.2)$$

where we add two ringdown curves to account for energy dissipation from one mode into another mode and to compensate for not exactly hitting the right frequency when driving a certain mode. All measurements could be performed while the

turbo pump was connected and running, making it possible to reach comparably low pressures.

4.3.1. Qualitative comparison of Q at atmospheric pressure and vacuum

A first measurement was performed to check if, in agreement with the measurement shown in section 4.2.5, the quality factor does not significantly improve when going to lower pressures. During these measurements we also analyzed a peak at roughly 5 Hz which we did not check in previous measurements, since we did not identify it as being of mechanical origin. With the quadrant diode available we could leave the sample in landscape orientation and resolve the direction of beam displacement at the diode. To put this into context with previous experiments, the *vertical* beam displacement now corresponds to what before was visible in the *landscape* orientation and the *horizontal* displacement maps to the *portrait* orientation from before, except for the vertical displacement which cannot be seen in both directions but only in the *vertical* direction. Each drivable mode was only visible in one direction.

Just from looking at the ringdown time traces in figure 4.9 it is quite evident that in disagreement with the results obtained before (table 4.4), the ringdown time increases at lower vacua, showing an increase in Q. This is quantified in the following section.

4.3.2. Quality factor versus pressure

When repeating the measurement described above we had access to a stronger turbo pump. The pump itself did not allow to regulate the pressure to higher values than the lower limit by decreasing the rotation speed. We obtained higher pressures by using a needle valve and slowly flooding the chamber while pumping at the same time. We also checked different lengths of the tubing between the pump and the chamber (a *short* tube with 0.5 m, a *middle* tube with 2.0 m and a *long* tube with 2.5 m, which was fixed to the lab floor) to see if the vibrations of the pump add additional damping or driving to the sample. The results can be seen in figure 4.10.

One can clearly see an improvement of mechanical quality for all frequencies when approaching low pressures; however by no means impressive, especially not on a log-lin scale. For 5 Hz, Q barely exceeds 20.

Another thing to notice here is the scattering of the data points and the small errors for Q. Since the errors were directly obtained from the ringdown fits, this indicates a low reproducibility of the experiment and possibly systematic errors.

When comparing the quality factors obtained for different tube lengths, it is not evident if the pump vibration adds a damping mechanism. We discuss the possibility for noise-induced damping in section 6.3. However, for the majority of data points the difference between the long tube and the middle tube seems to be small, which
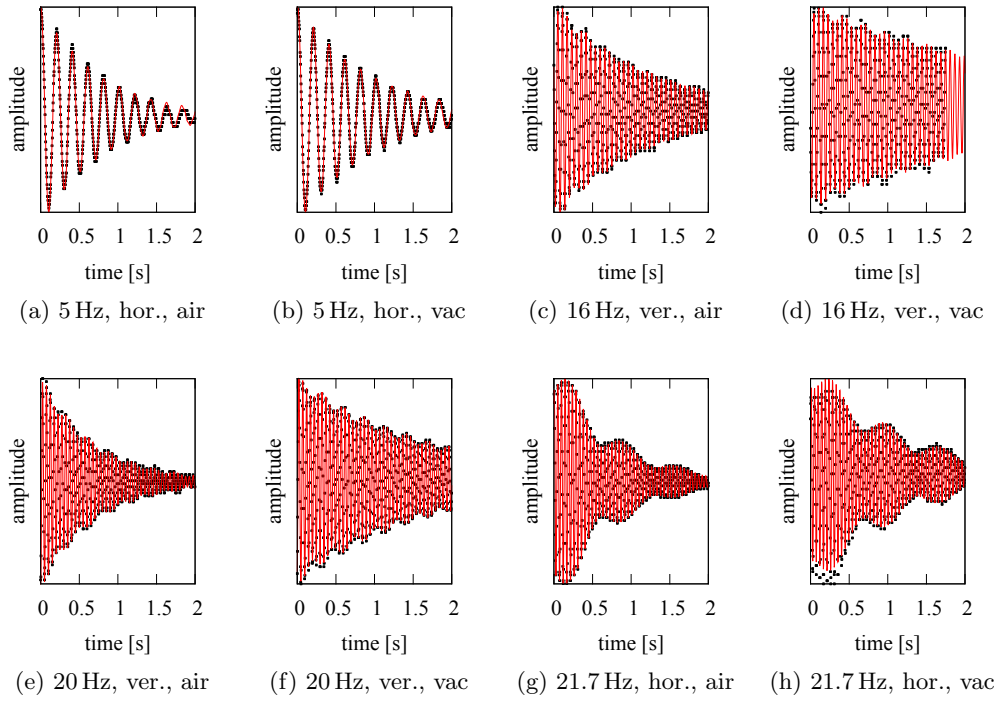
Figure 4.9.: Typical ringdown curves for driving frequencies of 5 Hz, 16 Hz, 20 Hz and 21.7 Hz. Red curves are fitted double ringdowns as in (4.2). Only every third data point is shown. *hor.* and *ver.* denote horizontal and vertical beam spot displacement direction; *air* and *vac* denote atmospheric pressure and a vacuum of about 10^{-2} mBar.

(a) 5 Hz

(b) 16 Hz

(c) 20 Hz

(d) 21.7 Hz
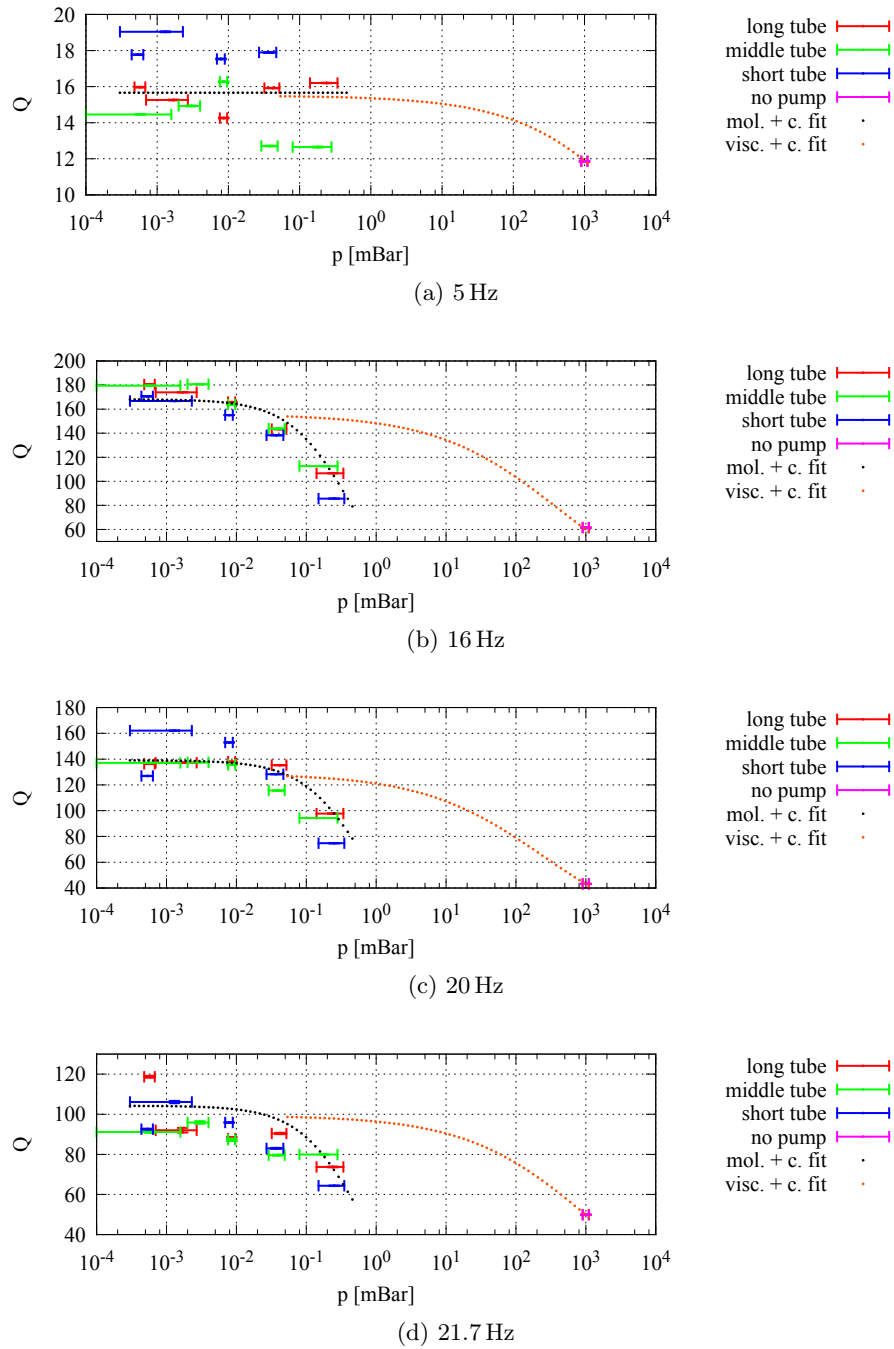
Figure 4.10.: Q versus P from ringdown measurements. The fitted curves are explained in section 6.1.

indicates that with the long tube the pump noise is damped out to a point where it does not significantly limiting the mechanical quality.

It is legitimate to ask why we see a significant increase of Q when going to lower pressures, which we did not see in the lock-in scans (section 4.2.5). This might be explainable with fluctuations in the phase picked up by the lock-in amplifier. Since the frequencies of the system are comparably low, the lock-in electronics might not be able to always get a sharp phase signal, which eventually could lead to broadened peaks. Alternatively, the frequencies of the system could vary during the measurements which would also lead to broadened peaks. Since the amplitudes occurring in lock-in measurements are large, one might also push the oscillator into non-linear regimes where the potential is not harmonic. Whatever the reason is, it seems safe to say that the broadening of the peaks in the lock-in measurements prohibits that method from giving trustable results for the quality factor.

4.4. Conclusion of the experiments

We identified four mechanical frequencies in the system: 5.0 Hz, 16.2 Hz, 20.0 Hz and 21.7 Hz. The second and fourth frequency seem to correspond to tilting modes of the pyrolytic graphite, while the third frequency is connected to a vertical translation.

We checked the mechanical quality of the different modes at atmospheric pressure and at different vacua. We saw a slight increase of Q at low pressures, but way below our expectation. This might be due to a effect of energy dissipation through induced eddy currents in the graphite, as implied by a measurement were we induced additional currents using aluminum foil on the sample and saw Q drop.

In the following sections we work out a theoretical framework to describe the mechanical frequencies and modes as well as the damping effects seen in the experiments.

5. Numerical simulation of levitated diamagnets

There have been some attempts on modeling diamagnetic levitation systems by drastically simplifying the geometry of the setup (e.g. by approximating a living frog as being pointlike [21]).

Instead of searching for approximation schemes to get analytical closed expressions, we work towards a full mechanical model of the experimental situation, which can then be evaluated numerically. The model is based on the assumption that an explicit expression for the magnetic flux density $\boldsymbol{B}_0$ as defined below can be written down as a function of some coordinates suitable for a volume integration.

5.1. Potential energy

We need to know the total energy of a diamagnet with finite volume in a given magnetic flux density $\boldsymbol{B}_0$,[1] which is assumed to be static. The magnetic flux density $\boldsymbol{B}$ *inside* of the diamagnet is given by the sum of the magnetic field $\boldsymbol{H}$ and the magnetization $\boldsymbol{M}$:

$$\frac{\boldsymbol{B}}{\mu_0} = \boldsymbol{H} + \boldsymbol{M}.$$

For a diamagnet, $\boldsymbol{M}$ is directly related to $\boldsymbol{H}$ via

$$\boldsymbol{M} = \chi \boldsymbol{.} \boldsymbol{H}$$

where χ is a rank-2 tensor and $\boldsymbol{.}$ denotes a matrix product. From its definition, $\boldsymbol{H}$ is the same quantity inside and outside of the diamagnet since there is no magnetization outside. In other words, $\boldsymbol{B}_0 \neq \boldsymbol{B}$ but $\boldsymbol{H}_0 = \boldsymbol{H}$ since $\boldsymbol{M}_0 = 0$. Therefore

$$\boldsymbol{M} = \chi \boldsymbol{.} \frac{\boldsymbol{B}_0}{\mu_0}. \tag{5.1}$$

The energy of a point-like object with magnetic moment $\boldsymbol{m}$ in a magnetic flux density $\boldsymbol{B}_0$ is given by [17, chapter 15]

$$V_{\mathrm{mag}} = -\boldsymbol{m} \cdot \boldsymbol{B}_0,$$

---

[1]In this part we refer to the field $\boldsymbol{B}$ as a *flux density* since we need the notion of a *magnetic field* for the quantity $\boldsymbol{H}$.

which can be generalized to a finite volume reintroducing the magnetization $\boldsymbol{M}$ as a *density of magnetic moment*:

$$V_{\text{mag}} = -\frac{1}{2} \int_V \boldsymbol{M}(\boldsymbol{x}) \cdot \boldsymbol{B}_0(\boldsymbol{x}) \mathrm{d}V,$$

where the integral needs to be carried out over the volume of the diamagnet and appropriate coordinates need to be chosen in order to be able to perform the integration. The factor $1/2$ is due to the fact that one has to integrate over magnetic *dipoles* which are counted twice.[2] With (5.1) this becomes

$$V_{\text{mag}} = -\frac{1}{2\,\mu_0} \int_V (\chi \boldsymbol{\cdot} \boldsymbol{B}_0(\boldsymbol{x})) \cdot \boldsymbol{B}_0(\boldsymbol{x}) \mathrm{d}V. \tag{5.2}$$

In articles where the tensor nature of χ is neglected one often finds the statement that the energy of the object is proportional to $\boldsymbol{B}_0^2$ and therefore does not depend on the field direction, but only on the magnitude. However, for pyrolytic graphite, the only diamagnet which (as a result of the model detailed here) can be levitated using just rare-earth magnets at room temperature, there is a factor of more than 10 between the components of χ. Eventually this leads to a significantly altered equilibrium position, as illustrated in figure 3.2 on page 10.

5.2. Equilibrium position

Since there is no rigid confinement, the diamagnetic object can have any position and any orientation in space. Therefore we have to account for six degrees of freedom denoted as

$$\tilde{\boldsymbol{q}} := \begin{pmatrix} \tilde{\boldsymbol{x}} \\ \tilde{\boldsymbol{\alpha}} \end{pmatrix} = (\tilde{x}_1, \tilde{x}_2, \tilde{x}_3, \tilde{\alpha}_1, \tilde{\alpha}_2, \tilde{\alpha}_3)^T$$

where α_1 is the (positive) rotation around the x_1 axis and so on. This is not a unique definition since the rotations do not commute. Instead we have to specify a transformation $\boldsymbol{\psi}$ moving the object according to the parameters:

$$\boldsymbol{x} \ \rightarrow \ \boldsymbol{x}' = \boldsymbol{\psi}\,(\boldsymbol{x}, \tilde{\boldsymbol{x}}, \tilde{\boldsymbol{\alpha}})$$

We need to apply two steps of transformation. In the first step we transform the object away from the origin to its equilibrium position $\boldsymbol{q}^* = (\boldsymbol{x}^*, \boldsymbol{\alpha}^*)$. In a second step described below, we apply a similar transformation to deflect the object from its equilibrium by $\tilde{q} = (\tilde{\boldsymbol{x}}, \tilde{\boldsymbol{\alpha}})$.[3]

---

[2]Another derivation of the factor was already shown in section 2.2.

[3]This treatment is not mandatory but convenient due to the noncommutativity of the degrees of freedom, which would make an approximation of the potential around the equilibrium position more complicated.

The transformation towards the equilibrium is defined as

$$\boldsymbol{\psi}^*(\boldsymbol{x}, \boldsymbol{x}^*, \boldsymbol{\alpha}^*) := \boldsymbol{x}^* + R_1(\alpha_1^*).R_2(\alpha_2^*).R_3(\alpha_3^*).\boldsymbol{x}$$

with rotation matrices in the Cartesian basis

$$R_3(\alpha) = \begin{pmatrix} \cos\alpha & -\sin\alpha & 0 \\ \sin\alpha & \cos\alpha & 0 \\ 0 & 0 & 1 \end{pmatrix}, \quad R_2(\alpha) = \begin{pmatrix} \cos\alpha & 0 & \sin\alpha \\ 0 & 1 & 0 \\ -\sin\alpha & 0 & \cos\alpha \end{pmatrix},$$

$$R_1(\alpha) = \begin{pmatrix} 1 & 0 & 0 \\ 0 & \cos\alpha & -\sin\alpha \\ 0 & \sin\alpha & \cos\alpha \end{pmatrix}.$$

Now we can write down the potential energy V_{mag} as a function of the position and orientation of the diamagnetic object:

$$V_{\mathrm{mag}}(\boldsymbol{x}^*, \boldsymbol{\alpha}^*) = -\frac{1}{2\,\mu_0} \int_V \left(\chi.\boldsymbol{B}_0(\psi^*(\boldsymbol{x}, \boldsymbol{x}^*, \boldsymbol{\alpha}^*)) \right) \cdot \boldsymbol{B}_0(\psi^*(\boldsymbol{x}, \boldsymbol{x}^*, \boldsymbol{\alpha}^*))\, \mathrm{d}V, \quad (5.3)$$

leading to a total energy

$$V(\boldsymbol{x}^*, \boldsymbol{\alpha}^*) = V_{\mathrm{mag}}(\boldsymbol{x}^*, \boldsymbol{\alpha}^*) + V_{\mathrm{g}}(x_3^*) \quad \text{with} \quad V_{\mathrm{g}}(x_3^*) = m\,g\,x_3^*. \quad (5.4)$$

Depending on the parameters and the magnetic flux density, this expression can have a local minimum which one can search numerically.[4] If the minimum lies within the permanent magnets or does not exist at all, the diamagnetic object cannot float.

5.3. Determination of frequencies and modes

If we have found an equilibrium position $\boldsymbol{q}^*$, we can apply Lagrangian mechanics to find the frequencies and eigenmodes of the system. In order to do that, we first apply a second transformation

$$\tilde{\boldsymbol{\psi}}(\boldsymbol{x}, \tilde{\boldsymbol{x}}, \tilde{\boldsymbol{\alpha}}, \boldsymbol{x}^*) := \tilde{\boldsymbol{x}} + \boldsymbol{x}^* + R_1(\tilde{\alpha}_1).R_2(\tilde{\alpha}_2).R_3(\tilde{\alpha}_3).(\boldsymbol{x} - \boldsymbol{x}^*)$$

which acts like a rotation around the center of mass by $\tilde{\boldsymbol{\alpha}}$ plus a displacement by $\tilde{\boldsymbol{x}}$. In order to simplify things, these rotations and translations are assumed to be small.

With this we can write down the kinetic energy as

$$T = \frac{1}{2}\,\dot{\tilde{\boldsymbol{q}}}^T.M.\dot{\tilde{\boldsymbol{q}}} = \frac{1}{2} \sum_{i,j=1}^{6} M_{ij}\,\dot{\tilde{q}}_i\,\dot{\tilde{q}}_j \quad \text{with} \quad M := \begin{pmatrix} m & & & \\ & m & & \\ & & m & \\ & & & I \end{pmatrix} \quad (5.5)$$

---

[4]If the geometry has a certain symmetry, one might also just guess some of the equilibrium parameters.

where I is the inertial tensor of the object *at equilibrium position* in the *Cartesian basis* around its *center of mass*:

$$I = \frac{m}{V} \int_V (\boldsymbol{\psi}^*(\boldsymbol{x}, 0, \boldsymbol{\alpha}^*))^2 \, \mathbf{1}_3 - \boldsymbol{\psi}^{*T}(\boldsymbol{x}, 0, \boldsymbol{\alpha}^*) \boldsymbol{.} \boldsymbol{\psi}^*(\boldsymbol{x}, 0, \boldsymbol{\alpha}^*) \, \mathrm{d}x_1 \, \mathrm{d}x_2 \, \mathrm{d}x_3.$$

With the second transformation applied, the potential is written as

$$V_{\mathrm{mag}}(\tilde{\boldsymbol{x}}, \tilde{\boldsymbol{\alpha}}, \boldsymbol{x}^*, \boldsymbol{\alpha}^*) = -\frac{1}{2\,\mu_0} \int_V \left(\boldsymbol{\chi} \boldsymbol{.} \boldsymbol{B}_0(\boldsymbol{\psi}^*(\tilde{\boldsymbol{\psi}}(\boldsymbol{x}, \tilde{\boldsymbol{x}}, \tilde{\boldsymbol{\alpha}}, \boldsymbol{x}^*), \boldsymbol{x}^*, \boldsymbol{\alpha}^*)) \right) \cdot$$
$$\cdot \boldsymbol{B}_0(\boldsymbol{\psi}^*(\tilde{\boldsymbol{\psi}}(\boldsymbol{x}, \tilde{\boldsymbol{x}}, \tilde{\boldsymbol{\alpha}}, \boldsymbol{x}^*), \boldsymbol{x}^*, \boldsymbol{\alpha}^*)) \, \mathrm{d}V$$
$$V_{\mathrm{g}}(\tilde{x}_3, x_3^*) = m\,g\,(\tilde{x}_3 + x_3^*) \tag{5.6}$$

and again $V = V_{\mathrm{mag}} + V_{\mathrm{g}}$.

At the equilibrium position $\boldsymbol{x}^*, \boldsymbol{\alpha}^*$ all first derivatives of V need to vanish:

$$\left. \frac{\partial V(\tilde{\boldsymbol{q}}, \boldsymbol{q}^*)}{\partial \tilde{q}_i} \right|_{\tilde{\boldsymbol{q}}=0} = 0 \quad \forall\, i.$$

We approximate the potential as being harmonic in all degrees of freedom around the point $\boldsymbol{x}^*, \boldsymbol{\alpha}^*$:

$$V \approx V|_{\tilde{\boldsymbol{q}}=0} + \frac{1}{2} \sum_{i,j=1}^{6} \underbrace{\left. \frac{\partial^2 V}{\partial \tilde{q}_i \, \partial \tilde{q}_j} \right|_{\tilde{\boldsymbol{q}}=0}}_{D_{ij}} \tilde{q}_i \, \tilde{q}_j. \tag{5.7}$$

With this, the classical Euler-Lagrange equations

$$\frac{\mathrm{d}}{\mathrm{d}t} \frac{\partial L}{\partial \dot{\tilde{q}}_k} - \frac{\partial L}{\partial \tilde{q}_k} = 0, \quad L = T - V, \quad k = 1, \ldots, 6$$

take the form

$$M_{kj}\,\ddot{\tilde{q}}_j + D_{kj}\,\tilde{q}_j = 0, \quad k = 1, \ldots, 6,$$

where we have used the symmetry of M_{ij} and D_{ij}. Making the ansatz

$$\tilde{\boldsymbol{q}}(t) = \boldsymbol{\xi}\,\mathrm{e}^{\mathrm{i}\,\omega\,t}$$

leads to the eigenvalue/eigenvector equation

$$\left(-\omega^2\,M + D\right) \boldsymbol{.} \boldsymbol{\xi} = 0 \tag{5.8}$$

which can be solved with standard algorithms and yields the desired frequencies and modes.

5.4. Application to the experimental setup

In order to evaluate the integral in (5.3) we need an explicit form of the magnetic field of a checkerboard-array of four cuboid magnets. The magnetic field $\boldsymbol{B}^{\square}$ of a single cuboid with dimensions $\boldsymbol{l} = (l_1, l_2, l_3)$ and uniform magnetization M_0 in x_3 direction is given by [27]

$$B_{1,2}^{\square}(\boldsymbol{x}) = \frac{\mu_0\,M_0}{4\pi} \sum_{k_{1,2,3}=1}^{2} (-1)^{k_1+k_2+k_3} \ln\left[x_{2,1} + (-1)^{k_{2,1}}\,l_{2,1}/2 + \kappa(\boldsymbol{x},\boldsymbol{k})\right]$$

$$B_3^{\square}(\boldsymbol{x}) = -\frac{\mu_0\,M_0}{4\pi} \sum_{k_{1,2,3}=1}^{2} (-1)^{k_1+k_2+k_3} \arctan\left[\frac{\prod_{j=1}^{2}\left(x_j + (-1)^{k_j}\,l_j/2\right)}{(x_3 + (-1)^{k_3}\,l_3/2)\,\kappa(\boldsymbol{x},\boldsymbol{k})}\right]$$

$$\kappa(\boldsymbol{x},\boldsymbol{k}) = \sqrt{\sum_{j=1}^{3}\left(x_j + (-1)^{k_j}\,l_j/2\right)^2}.$$

In an approximation, the field of the checkerboard array is a superposition of four single cuboid fields[5]

$$\boldsymbol{B}^{\boxplus}(\boldsymbol{x}) \approx \sum_{i_{1,2}=0}^{1} (-1)^{i_1\,i_2}\,\boldsymbol{B}^{\square}\left(\boldsymbol{x} + \left((-1)^{i_1}\,l_1/2, (-1)^{i_2}\,l_2/2, 0\right)^T\right).$$

All experimental parameters are listed in table 3.1 on page 8 and table 3.2 on page 9. For the magnetization we used $M_0 = 900 \cdot 10^3\,\text{A/m}$.

The equilibrium position $\boldsymbol{q}^*$ is numerically found to be[6]

$$\boldsymbol{x}^* = \begin{pmatrix} 0 \\ 0 \\ 6.59 \end{pmatrix} \text{mm}, \quad \boldsymbol{\alpha}^* = \begin{pmatrix} 0 \\ 0 \\ \pi/4 \end{pmatrix} \text{rad}$$

using equations (5.3) and (5.4), where the integration was carried out in Cartesian coordinates over the volume of the piece of pyrolytic graphite with dimensions $\boldsymbol{s}$ and susceptibility tensor χ as given in table 3.1. This corresponds to a levitation height of $6.59\,\text{mm} - l_3/2 = 0.59\,\text{mm}$, which agrees with the measured value $(0.5[2]\,\text{mm})$. Again, note that the *diagonal* equilibrium orientation is due to the anisotropy of the graphite.

---

[5]This is not exact since the magnets change each others respective magnetization and the field can also be amplified by surrounding paramagnets.

[6]All values except for x_3^* initially have been guessed. It was then later verified that this position corresponds to a local minimum by checking the positive definiteness of the Hesse matrix D of V as defined in (5.7).

When calculating the Hesse matrix D of V as in (5.7), it turned out that straight-forward numerical differentiation was not possible and numerical integration of double derivatives of the integrand of (5.6) did not converge. Eventually we ended up with approximating the Hesse matrix of the integrand within the volume at equilibrium position by using interpolated functions with 9 interpolation points in x_1 and x_2 directions and 5 points in x_3 direction (figure 5.1), which takes about 15 minutes on a well equipped desktop PC. After this, integration can be done within seconds.

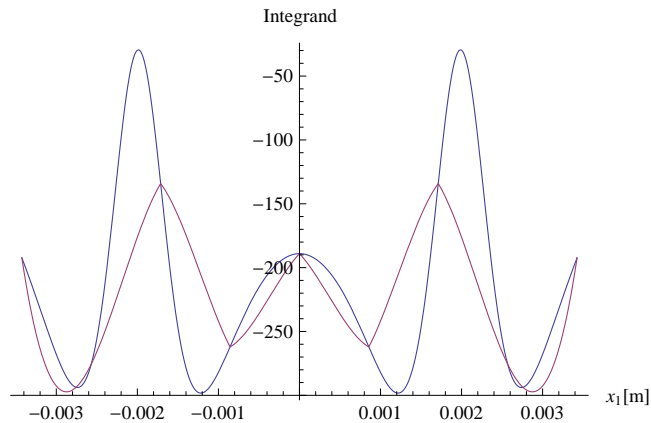Figure 5.1.: Comparison between the second derivative in x_3 of the original integrand expression (blue) and an interpolating function (red) at a random x_1 and x_2 coordinate within the sample. Clearly one should use more points; however, the area below the curve, which one obtains from integration, is approximately equal for both curves.

With M as in (5.5) and D as in (5.7) known, evaluation of (5.8) is possible,

yielding

$$
\boldsymbol{\xi}_I = \begin{pmatrix} -0.018\,\mathrm{m} \\ 0.018\,\mathrm{m} \\ 0 \\ 0.71\,\mathrm{rad} \\ 0.71\,\mathrm{rad} \\ 0 \end{pmatrix}, \quad \omega_I \approx 2.7\,\mathrm{Hz}; \quad \boldsymbol{\xi}_{II} = \begin{pmatrix} 0.028\,\mathrm{m} \\ 0.028\,\mathrm{m} \\ 0 \\ -0.71\,\mathrm{rad} \\ 0.71\,\mathrm{rad} \\ 0 \end{pmatrix}, \quad \omega_{II} \approx 3.2\,\mathrm{Hz};
$$

$$
\boldsymbol{\xi}_{III} = \begin{pmatrix} 0 \\ 0 \\ 0 \\ 0 \\ 0 \\ 1\,\mathrm{rad} \end{pmatrix}, \quad \omega_{III} \approx 4.8\,\mathrm{Hz}; \quad \boldsymbol{\xi}_{IV} = \begin{pmatrix} 0.14 \cdot 10^{-3}\,\mathrm{m} \\ -0.14 \cdot 10^{-3}\,\mathrm{m} \\ 0 \\ 0.71\,\mathrm{rad} \\ 0.71\,\mathrm{rad} \\ 0 \end{pmatrix}, \quad \omega_{IV} \approx 21.5\,\mathrm{Hz};
$$

$$
\boldsymbol{\xi}_V = \begin{pmatrix} 0 \\ 0 \\ 1\,\mathrm{m} \\ 0 \\ 0 \\ 0 \end{pmatrix}, \quad \omega_V \approx 22.7\,\mathrm{Hz}; \quad \boldsymbol{\xi}_{VI} = \begin{pmatrix} -0.07 \cdot 10^{-3}\,\mathrm{m} \\ -0.07 \cdot 10^{-3}\,\mathrm{m} \\ 0 \\ 0.71\,\mathrm{rad} \\ 0.71\,\mathrm{rad} \\ 0 \end{pmatrix}, \quad \omega_{IV} \approx 23.4\,\mathrm{Hz};
$$

where the vectors were normalized to have a numerical length of 1 in the given units. The modes are visualized in figure 5.2.

5.5. Comparison of simulation and experiment

If we identify the frequencies measured in the experiment with modes from the simulation as done in table 5.1, we find a trend towards correspondence of the simulated modes with the measured modes we inferred as described in section 4.2.2.

The simulation qualitatively gives the right order of the modes (when sorted by frequency) but gives slightly too high frequencies. This could be explained by the magnetization of the permanent magnets used for the calculation, which is only given as a broad range (table 3.2, page 9). One could verify this using a Hall probe.

It is hard to say which mode corresponds to the 5 Hz peak we could drive in the ringdown measurements. This could be answered by lock-in scans with a quadrant diode in the sub-10 Hz region with long integration times, where at least one more mechanical peak should show up which should have approximately the same (very low) Q as the 5 Hz mode.
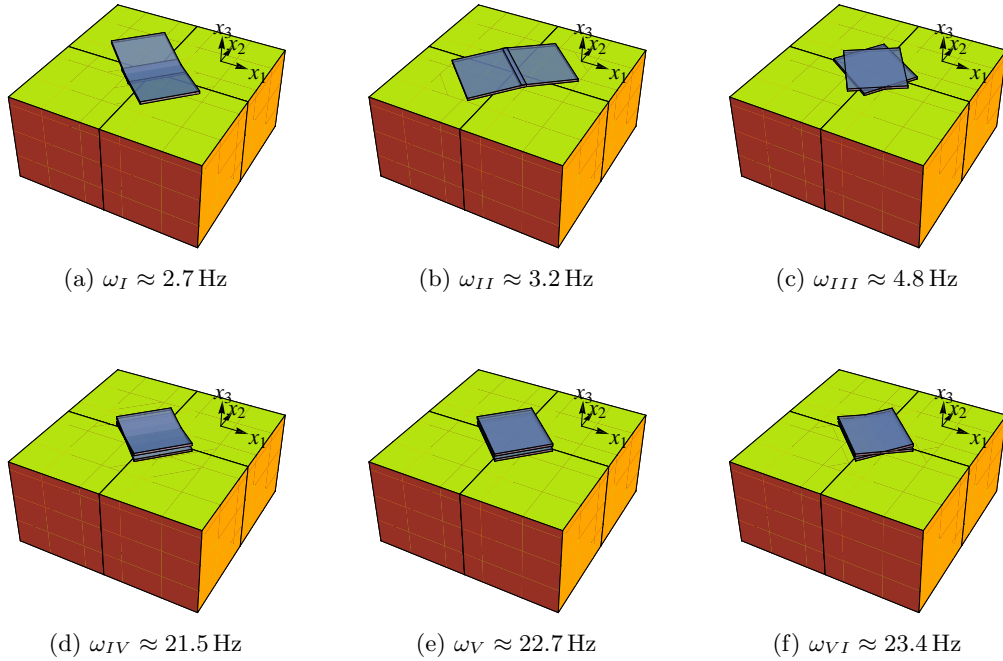
(a) $\omega_I \approx 2.7\,\mathrm{Hz}$ (b) $\omega_{II} \approx 3.2\,\mathrm{Hz}$ (c) $\omega_{III} \approx 4.8\,\mathrm{Hz}$

(d) $\omega_{IV} \approx 21.5\,\mathrm{Hz}$ (e) $\omega_V \approx 22.7\,\mathrm{Hz}$ (f) $\omega_{VI} \approx 23.4\,\mathrm{Hz}$

Figure 5.2.: Visualized mechanical modes of the sample.
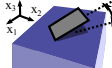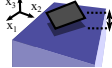
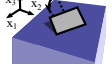| ω_{exp} [Hz]	inferred mode	ω_{sim} [Hz]	computed mode
16.2		21.5	figure 5.2d
20.0		22.7	figure 5.2e
21.7		23.4	figure 5.2f

Table 5.1.: Comparison between the measured frequencies and the inferred modes and the corresponding numerically found modes

5.6. Application to other samples

5.6.1. Levitation of different diamagnets

With this simulation, we could not find *any* other (known) material (e.g. bismuth, diamond) in combination with *any* rare-earth magnet geometry which would allow for levitation. This statement agrees with the fact that we could not find publications on rare-earth magnet levitation of any diamagnet which is not pyrolytic graphite. However, to our knowledge there is no known proof of this, and with the development of new diamagnetic materials and stronger permanent magnets it could be possible to levitate other diamagnets than graphite in the future.

Bismuth can be used for diamagnetically stabilized levitation of a permanent magnet and even the diamagnetism of the water inside human fingers is strong enough to stabilize perma-magnetic levitation if one has a very strong lifter magnet [22]. However, this situation is not comparable to the case of levitation of a diamagnet, since the density of bismuth is much higher than that of graphite, which matters when bismuth is levitated but of course does not matter when it is fixed and just used for stabilization of another levitator.

5.6.2. Smaller magnets

When we plug in the properties of the nickel-coated magnets used in the experiment (section 4.2.8) we get the frequencies listed in table 5.2.

magnet side length [mm]	f_1 [Hz]	f_2 [Hz]	f_3 [Hz]
10 (simulated)	21.6	22.8	23.4
10 (measured)	17.42[1]	20.52[4]	21.48[2]
12 (simulated)	21.5	22.8	23.4
12 (measured)	16.59[2]	20.07[2]	21.56[2]

Table 5.2.: Comparison of magnet-size dependence in the experiment and the numerical simulation.

Surprisingly, the frequency estimates from the simulation do only change slightly for the smaller magnet geometry, which could be explained by the fact that the magnetization of the permanent magnets is the same in both cases and the sample size is small compared to the dimensions of the permanent magnets. It could also indicate that the stray of magnetization of the commercial permanent magnets is bigger than any changes in the frequencies caused by the geometry.

5.6.3. Different mass

Increasing the weight to $64.4\,\text{mg}$ and $67.0\,\text{mg}$ similar to the performed experiment yields the frequencies listed in tab. 5.3.

sample mass [mg]	f_1 [Hz]	f_2 [Hz]	f_3 [Hz]
61.5 (simulated)	21.5	22.8	23.4
61.5 (measured)	16.26[1]	19.93[2]	21.48[3]
64.4 (simulated)	21.7	23.0	23.7
64.4 (measured)	16.05[2]	19.98[2]	
67.0 (simulated)	21.4	22.5	23.3
67.0 (measured)	15.74[2]	20.11[2]	21.16[2]

Table 5.3.: Comparison of sample-mass dependence in the experiment and the numerical simulation.

From these three points of data, it is clearly not possible to evaluate if the experimentally observed behavior of the sample agrees with the model. A test with more weight- and data points would lead to a more interpretation-friendly set of results; however, performing these measurements was missed during the time frame of this thesis.

5.6.4. Mechanical dependence on magnetization

To see if we can reproduce the frequencies seen in the experiment with our model by just adjusting the magnetization M_0, we checked the frequencies of the individual modes for a range of magnetizations (figure 5.3). Interestingly, for magnetizations below $850\,\text{kA/m}$ the equilibrium position changes in all degrees of freedom, making it hard to numerically determine if the sample can still levitate. For higher magnetizations we see that we are not able to reproduce the $16.2\,\text{Hz}/20.0\,\text{Hz}/21.7\,\text{Hz}$ frequencies. Also, the levitation height obtained for $M_0 = 2 \cdot 10^6\,\text{A/m}$ is $1.6\,\text{mm}$, which is way above the height we saw in the experiment. Therefore, more parameters than just the magnetization would have to be adjusted in order to reproduce the experimental values; assuming the model is correct. The obvious candidate for further adjustments would be the susceptibility tensor of the pyrolytic graphite.

5.6.5. A superconductor scheme

We use the model to determine the frequencies of the vertically displaced mode for a superconductor levitation scheme. The sample was assumed to be a square cuboid of superconducting lead ($\chi = -1$) with a thickness of $50\,\mu\text{m}$ and the side lengths given in table 5.4. For the suspension we took the numbers from the same ordinary
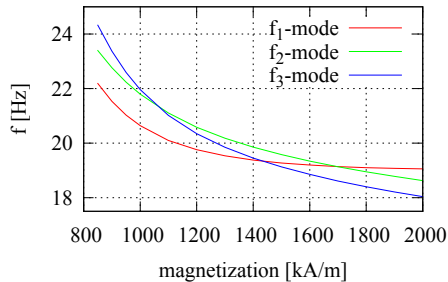
Figure 5.3.: Dependence of mechanical frequencies on the magnetization M_0 of the permanent magnets as obtained from the model.

rare-earth magnets as before (here, with a side length of $2\,\text{mm}$), but in a *double array* configuration where above the lower checkerboard array we stack the same array, but with magnetization pointing to the opposite direction and leave a gap of $150\,\mu\text{m}$ between the two arrays (figure 5.4).
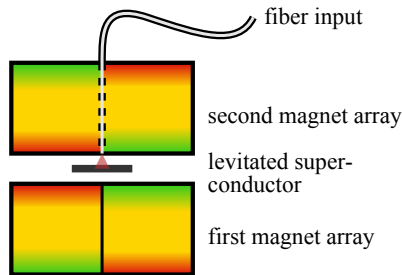

Figure 5.4.: A possible scheme to achieve higher oscillation frequencies using superconductors and a double magnet array.

side length [μm]	weight [μg]	ω_{sim} [Hz]
400	91	10077
200	23	10244
100	6	does not levitate

Table 5.4.: Numerical estimations for frequencies of the x_3 mode in a superconductor levitation scheme.

The optical addressing of the sample would need to happen with a fiber, where the fiber runs through the magnets. Still, looking at the estimated frequencies, the stiffness of the trap is comparably weak even in a double-trap with a levitated

superconductor.

6. Estimations on damping

6.1. Air drag damping

In order to quantify the damping which is *not* due to air drag, we need an expression for the air drag first. The treatment for air drag damping mechanisms explained here follows that of [28].

It is useful to differ between two pressure regions: In the *viscous region*, the mean free path length of the air molecules is smaller than the sample size, and the air acts like a fluid. In the *molecular region* the mean free path length is larger and one has to account for kicks of single molecules.

The mean free path length is given by

$$\Lambda(P) = \frac{\mu}{P} \sqrt{\frac{2\,k_B\,T}{m_{\mathrm{air}}}}$$

where $\mu = 18.239 \cdot 10^{-6}\,\mathrm{s\,Pa}$ is the viscosity of air at $T = 295\,\mathrm{K}$ and $m_{\mathrm{air}} = 48.1 \cdot 10^{-27}\,\mathrm{kg}$ is the (average) mass of an air molecule. The typical sample size is about $5\,\mathrm{mm}$, resulting in a critical pressure of about $1.5\,\mathrm{Pa}$.

The quality factor limit from air drag damping follows

$$Q = \rho_s\,b\,d\,\omega / f_1(P) \tag{6.1}$$

where ρ_s is the density of the sample, b is its width, d its thickness and $f_1(P) = \beta_1(P)/l$ the dissipative drag per unit length.[1]

6.1.1. Molecular damping

In the molecular regime,

$$f_1(P) = k_m(P)\,b\,P \quad \text{with} \quad k_m(P) = \frac{4}{3}\sqrt{\frac{2\,m_{\mathrm{air}}}{\pi\,k_B\,T}}$$

---

[1] From the dimensions involved it seems questionable if the treatment, which is adopted from cantilever beams, can actually be correct for a levitated object. However, the final expressions are general and not restricted to a certain cantilever geometry.

which inserted into (6.1) gives

$$Q(P) = \frac{3}{4} \sqrt{\frac{\pi}{2} \frac{k_B T}{m_{\mathrm{air}}}} \, \rho_s \, d \, \omega \frac{1}{P}$$
$$= \frac{3}{4} \sqrt{\frac{\pi}{2} \frac{k_B T}{m_{\mathrm{air}}}} \, \frac{m_s \, \omega}{A} \frac{1}{P}, \tag{6.2}$$

where A is the face area of the plate.

6.1.2. Viscous damping

In the viscous regime,

$$\beta_1(P) = 6\pi \, \mu \, R \left(1 + \frac{R}{\delta(P)} \right)$$

where δ is the width of a boundary layer perpendicular to the direction of the motion and is a measure for the depth of penetration of a lateral wave,

$$\delta(P) = \sqrt{\frac{2 \, \mu}{\rho_0(P) \, \omega}},$$

and R is the radius of a sphere which approximates the object. For an ideal gas, $\rho_0(P) = \frac{m_{\mathrm{air}}}{k_B T} P$. Insertion into (6.1) yields

$$Q(P) = \frac{\rho_s \, b \, d \, l \, \omega}{6 \, \pi \, \mu \, R} \frac{1}{1 + R \sqrt{\frac{\omega}{2 \, \mu} \frac{m_{\mathrm{air}}}{k_B T}} \sqrt{P}}$$
$$= \frac{m_s \, \omega}{6 \, \pi \, \mu \, R} \frac{1}{1 + R \sqrt{\frac{\omega}{2 \, \mu} \frac{m_{\mathrm{air}}}{k_B T}} \sqrt{P}}. \tag{6.3}$$

It is important to note that the effective air drag damping is not a superposition of the two mechanisms; just one of them is active depending on the pressure. From (6.3), the quality factor from viscous damping does not diverge (as it should) when the pressure goes to zero. Therefore the formula cannot be valid for very low pressures.

6.1.3. Adoption to measurement data

The model for air-damping is fitted to the data given in section 4.3.2 (figure 4.10). All parameters except for R, which should be in the mm range, are known. However, the molecular damping treatment does only apply strictly for the direction of motion orthogonal to the plane, hence we also include the surface A in the fitted parameters

to get an effective surface for each respective mode. Since we expect at least one other damping mechanism as stated above, the function fitted is

$$Q_{\text{total}}(P) = \frac{1}{\frac{1}{Q_{\text{air}}(P)} + \frac{1}{Q_{\text{other}}}}$$

where we used the addition of quality factors from (A.4) and Q_{other} summarizes the limiting Q of all damping mechanisms which do not depend on pressure.

For each frequency, we first fit the molecular damping (6.2) through the points below 1 mbar[2] using the parameters A and Q_{other}. Then we fit the viscous damping (6.3) through the point at atmospheric pressure and the point for the highest pressure below 1 bar using the parameter R with Q_{other} fixed from the fit done before. The fitted curves are shown in figure 4.10 on page 28 and the results are collected in table 6.1.

f [Hz]	Q_{other}	A [mm^2]	R [mm]
5	15.6[4]		14.8[13]
16	168.2[55]	310[37]	10.7[25]
20	139.1[20]	257[31]	13.1[10]
21.7	104.2[74]	361[103]	10.6[3]

Table 6.1.: Fit results for air damping mechanism.

Since A and R have to be seen as *effective* values for the respective modes, it is not surprising that they vary from frequency to frequency. One should note that other damping mechanisms, such as eddy currents (section 6.2), also depend on the mode and therefore their respective Q does not need to be identical for different frequencies. The important thing to note here is that the data points obtained from the ringdown measurements cannot solely be explained by air damping and there is at least one other damping mechanism, which ultimately limits Q. This can even directly be seen from the data, since without other damping mechanisms a pressure decrease from 10^{-2} mbar to 10^{-3} mbar would increase Q by a factor of 10 (since in the molecular regime, $Q \propto 1/P$). A plot of Q versus p as one would expect if there were no additional damping mechanisms is shown in figure 6.1.

6.2. Eddy current damping

We try to find an estimation for the eddy currents induced in the pyrolytic graphite through its motion in the magnetic field. These eddy currents will induce damping

---

[2]Even though one or two per set of those points do not lie in the molecular regime, we included them for fitting since the fit worked well and the boundary between the viscous and the molecular regime is not sharp.
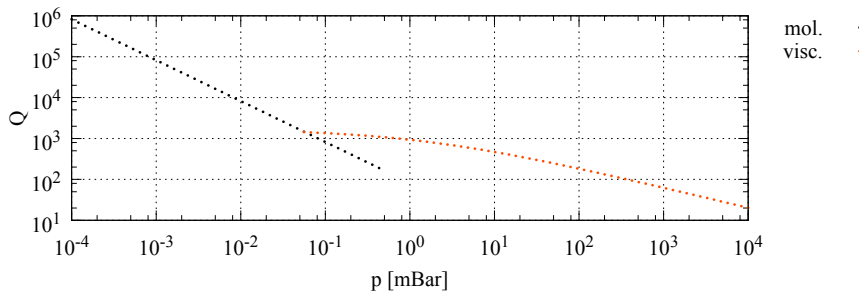
Figure 6.1.: Behavior of air damping *without* additional damping mechanisms with parameters A and R obtained from the fit to the 20 Hz mode data (table 6.1). Please note the logarithmic scale for Q (as opposed to the linear scale in figure 4.10).

as effectively energy is transfered from the motion to these currents which cause heating due to the finite resistance of the graphite. We start by writing down the electric field $\boldsymbol{E}'$ seen by an observer moving with the graphite,

$$\boldsymbol{E}' = \boldsymbol{E} + \boldsymbol{v} \times \boldsymbol{B}$$

where $\boldsymbol{E}$ is the electric field seen by a fixed observer, $\boldsymbol{v}$ is the velocity and $\boldsymbol{B}$ is the magnetic field. From the definition of the *conductivity tensor* σ as the factor between the *current density* $\boldsymbol{J}$ and the electric field, $\boldsymbol{J} = \sigma.\boldsymbol{E}$, we write

$$\boldsymbol{J}' = \sigma_{\boldsymbol{\cdot}} \left(\boldsymbol{E} + \boldsymbol{v} \times \boldsymbol{B} \right).$$

The electric field $\boldsymbol{E}$ arises through surface charges which are pushed towards the edges of the volume. This field influences the moving charges and changes the effective current density on the faces of the volume to be zero orthogonal to each respective face. Therefore, there are not currents into or out of the volume, which is required since the volume is surrounded by vacuum.

The effect of surface charges has to be individually modeled for a given symmetry. This has been done for a cylinder symmetry in [29]. Unfortunately, the result obtained in the reference is by no means applicable to our setup.[3] As a first approximation we set the surface currents to zero by multiplying the components of $\boldsymbol{J}$

---

[3]For a cylinder symmetry, one finds that the total radial current density $\boldsymbol{J}'_r(r, \phi, z)$ is obtained by taking the radial current density without the electric field $\boldsymbol{J}_r(r, \phi, z) = \boldsymbol{v} \times B$ and subtracting the mirrored current density at the double radius $2\,R$, $\boldsymbol{J}_r(2\,R - r, \phi, z)$. This fulfills $\boldsymbol{J}'_r(r, \phi, z) = \boldsymbol{J}_r(r, \phi, z) - \boldsymbol{J}_r(2\,R - r, \phi, z) = 0$ at $r = R$, so at the surface there are no radial currents. Adopting this result for our symmetry fails since subtraction of mirrored currents to fulfill the boundary condition eventually leads to a wrong sign of $\boldsymbol{J}'$ and cannot be done with opposite non-symmetrical boundaries.

with a cosine function which is zero at the boundaries. Our $\boldsymbol{J}'$ is then given by

$$\boldsymbol{J}'(\boldsymbol{x}) = \begin{pmatrix} \cos(\pi/2\, x_1/s_1)\, J_1(\boldsymbol{x}) \\ \cos(\pi/2\, x_2/s_2)\, J_2(\boldsymbol{x}) \\ \cos(\pi/2\, x_3/s_3)\, J_3(\boldsymbol{x}) \end{pmatrix}$$

with $\boldsymbol{s}$ as in table 3.2. A plot of $\boldsymbol{J}$ and $\boldsymbol{J}'$ can be seen in figure 6.2.

(a) $J_1(\boldsymbol{x})$ (b) $J_1'(\boldsymbol{x})$ (c) $J_2(\boldsymbol{x})$ (d) $J_2'(\boldsymbol{x})$

(e) $\boldsymbol{J}(\boldsymbol{x})$ (f) $\boldsymbol{J}'(\boldsymbol{x})$
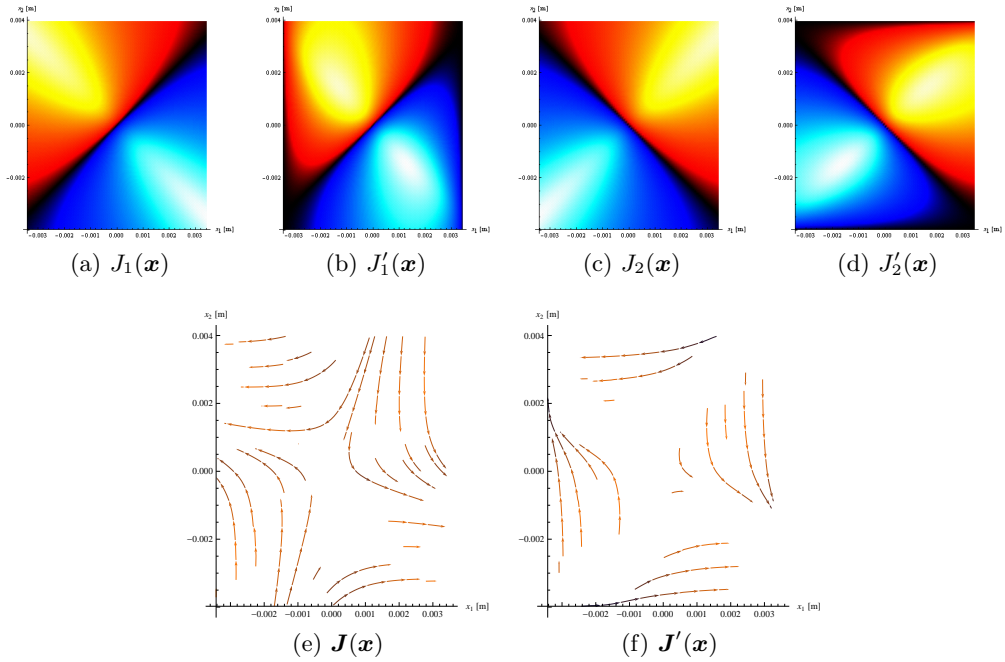
Figure 6.2.: Comparison of $\boldsymbol{J}$ and $\boldsymbol{J}'$ in the x_1-x_2 plane. The modified J' fulfills the boundary condition that currents orthogonal to the faces of the volume must vanish.

The force resulting from the currents is given by the magnetic force (often referred to as *Lorentz force*)

$$\boldsymbol{F} = \int_V \boldsymbol{J}' \times \boldsymbol{B} \, \mathrm{d}V,$$

where the integration is carried out over the volume of the object.

Let us focus on the x_3 mode which has a frequency of roughly $20\,\mathrm{Hz}$. We write

$$\boldsymbol{v} = v \begin{pmatrix} 0 \\ 0 \\ 1 \end{pmatrix}.$$

If we transform the magnetic field inside of the integration volume, we can perform the integration in the Cartesian basis and write down the conductivity tensor σ as a diagonal matrix with entries σ_1, σ_2, σ_3. Then the expression for the force evaluates to

$$\boldsymbol{F} = -v \int_V \begin{pmatrix} -\sigma_2 \, B_1 \, B_3 \\ -\sigma_1 \, B_2 \, B_3 \\ \sigma_1 \, B_2^2 + \sigma_2 \, B_1^2 \end{pmatrix} \mathrm{d}V$$

where one has to evaluate every component of $\boldsymbol{B}$ at the equilibrium coordinates $\boldsymbol{\psi}^*(\boldsymbol{x}, \boldsymbol{x}^*, \boldsymbol{\alpha}^*)$, i.e. $B_i = B_i(\boldsymbol{\psi}^*(\boldsymbol{x}, \boldsymbol{x}^*, \boldsymbol{\alpha}^*))$. When the integrated volume is centered around any point on the x_3-axis, due to the symmetry of the magnetic field the $B_1 \, B_3$ and $B_2 \, B_3$ terms will vanish in the integration and the resulting force only has a non-zero x_3 component. Using (A.1) and (A.3), we find

$$Q = \frac{m \, \omega_0}{F_3} = \frac{m \, \omega_0}{\int_V \left(\sigma_1 \, B_2^2 + \sigma_2 \, B_1^2 \right) \mathrm{d}V}. \tag{6.4}$$

The conductivity of pyrolytic graphite is[4]

$$\sigma = \begin{pmatrix} 1/\left(4{\cdot}10^{-6} \, \Omega\mathrm{m}\right) & & \\ & 1/\left(4{\cdot}10^{-6} \, \Omega\mathrm{m}\right) & \\ & & 1/\left(10^{-3} \, \Omega\mathrm{m}\right) \end{pmatrix}.$$

Numerical evaluation of (6.4) yields $Q_{\mathrm{eddy,graphite}} \approx 13.5$.

The piece of aluminum foil used for additional damping has properties listed in table 4.6 on page 24. If it was oscillating with a frequency of $20\,\mathrm{Hz}$ and had the same mass as the graphite sample[5], the limiting quality factor of just the aluminum would be $Q_{\mathrm{eddy,alu}} \approx 2.9$.

When compared to the experiment, these values are certainly too small. For the x_3 mode at $20\,\mathrm{Hz}$, the limiting Q from eddy currents in the graphite should be 139.1 (table 6.1) if there are no damping mechanisms but air and eddy currents while the numerical approximation gives 13.5. For the aluminum, it is a Q of 15.0 from the lock-in measurements (table 4.7) and 2.9 from the numerical approximation. The factors between the prediction and the measured values are 10 for the graphite and 5 for the aluminum. This indicates that the image charge mechanism, which we more or less neglected, has a huge impact on the currents in the sample and needs to be further investigated, i.e. by either finding a full analytical treatment or by

---

[4] *European Carbon and Graphite Association,* http://www.carbonandgraphite.org/pdf/graphite_production.pdf. These values represent the lower conductivity boundary of the values given in the source.

[5] This appears strange, but if the mass of the aluminum is small against the mass of the sample, which is the case, this corresponds to the damping ratio difference of the sample without and with aluminum, as calculated in the last column of table 4.7.

performing a finite-element simulation of this problem. However, it is quite evident that indeed eddy currents lead to a significant and most-likely dominant dissipation mechanism in the investigated system.

6.3. Noise damping

In section 4.3.2 we saw that environmental noise, such as that of a vacuum pump, can decrease the effective mechanical quality of an oscillating system. This appears to be counter-intuitive but there are some arguments why this actually makes sense.

A possible explanation comes from comparison with air damping in the molecular regime. Both, environmental noise shaking the setup and molecules hitting the sample, can be described as random kicks from all directions. Since air damping is well understood, it is not surprising that environmental noise adds damping as well. However, the environmental kicks are less frequent but have a much higher amplitude than kicks of air molecules, so the two situations are not quite comparable.

Another argument relates to the change of the potential through noise kicks. In one dimension, a random kick will only change the position of the object within the potential, but not the frequency. However, in multiple dimensions a change of the position in one direction leads to a change of the effective potential seen in the other degrees of freedom. This change of frequency is a damping mechanism.

A more profound argument comes from interpreting the environmental noise as a bath that interacts with the system, which can lead to both inhomogeneous broadening and damping. In this case one could also check if Voigt profiles, which arise from the combination of a Lorentzian and a Gaussian broadening mechanism, give better error estimations for the fits for the data obtained in the lock-in measurements in section 4.2.

7. Wrap-up

7.1. Outlook

We provide some ideas on what could be done in the future in order to better understand the effects seen in the present experiment and to improve the setup to approach higher frequencies and mechanical qualities.

7.1.1. Improving magnet geometry

The checkerboard array of four magnets used throughout the experiments might not be the ideal solution in terms of stability and frequencies. Pieces of pyrolytic graphite also levitate on checkerboard arrays of more than four magnets (and can actually take an equilibrium position centered on one of them as shown in figure 7.1) or single toroidal magnets.

It would be comparably easy to increase the gradient in the magnetic field and thereby the frequency by having an identical magnet (-array) with opposite field direction above the levitated sample.
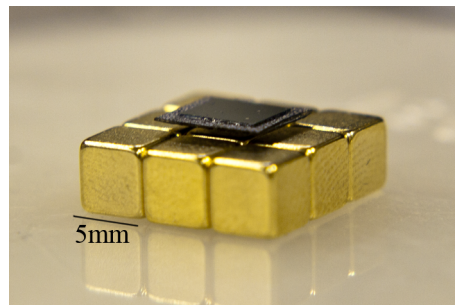
Figure 7.1.: Alternative levitation geometry.

7.1.2. Levitating superconductors

As described above, it could be possible to reach frequencies of about $10\,\text{kHz}$ in an *opto-magnetical* superconductor levitation experiment. The dominant damping mechanism in such an experiment is induced eddy currents in the permanent magnets, since in presence of a completely field-repelling diamagnet the field felt by the

magnets changes when the diamagnet moves. Also, the emission of electromagnetic waves due to aforementioned movement dissipates energy; however, those waves would have very low frequency. If one were to replace the permanent magnets with superconducting magnets, one could get rid of the eddy current damping effect and have a mechanical system almost completely free of damping. However, this system provides experimental challenges which need to be investigated in detail.

7.1.3. Mapping the current density

In order to better understand the induced currents, one could experimentally obtain a map the induced currents $\boldsymbol{J}$ in the x_1-x_2 plane. This could be done by fixing the graphite and moving the magnets. By taking the induced voltage between two points, one could create a map of the voltage throughout the sample. The gradient of this is the total electric field $\boldsymbol{E}$ which then gives the currents via $\boldsymbol{J} = \sigma\boldsymbol{.E}$.

7.2. Conclusion

We used three different measurement schemes along with models of the mechanical properties and the damping mechanisms to characterize the properties of a diamagnetically levitated system. We investigated if room-temperature diamagnetic levitation provides a feasible way for optomechanic experiments. The answer is most likely *no*. Even in high vacuum, damping through induced eddy currents prevents the only diamagnetic material which can be levitated at room temperature, pyrolytic graphite, from providing a high-quality mechanical system. To get rid of eddy currents, one would need either a non-conducting strong diamagnet, which has not yet been discovered, or a superconductor, which requires low temperatures.

Based on the results gathered throughout this thesis we suggest that further investigation should focus on superconductor mechanics schemes. There are some interesting things to discover, e.g. *magnetomechanics* where one could explore levitated diamagnets without the use of light, or levitation of a superconductor in suprafluid helium.

7.3. Acknowledgment

I want to thank Univ.-Prof. Dr. Markus Aspelmeyer for the supervision of this thesis, his great support in all respects and his efforts to create a scientific and social environment which is extremely motivating to work in.

Special thanks for heaps of helpful advice and inspiring discussions go to Dr. Nikolai Kiesel. Further I would like to thank Dr. Garrett Cole, Dr. Witlef Wieczorek and

A. Driven damped harmonic oscillator

We briefly describe the theory of a damped harmonic oscillator with external driving. This treatment is for the 1-dimensional case but can easily be generalized to multiple dimensions as soon as the decoupled eigenmodes are found.

A classical damped oscillator in a harmonic potential is described by a restoring force $-\alpha\,x$ and a damping force $-\beta\,\dot{x}$. It can also be driven by a force $F_{\text{ext}}(t)$. Since all forces together must equal $F_{\text{total}} = m\,\ddot{x}$, the equations of motion can be written as

$$m\,\ddot{x} + \beta\,\dot{x} + \alpha\,x = F_{\text{ext}}(t).$$

We rewrite this as

$$\ddot{x} + 2\,\zeta\,\omega_0\,\dot{x} + \omega_0^2\,x = \frac{F_{\text{ext}}(t)}{m} \tag{A.1}$$

where we have introduced the *damping ratio* $\zeta = \beta/(2\,\omega_0\,m)$ and the *eigenfrequency* $\omega_0 = \sqrt{\alpha/m}$.

For the full solution to the problem, one needs the general solution to the homogeneous problem (without driving) and a special solution for the inhomogeneous case (with driving).

The solution for the homogeneous case of (A.1) where $F_{\text{ext}} = 0$ is

$$x_{\text{hom}} = A\,\mathrm{e}^{-\zeta\,\omega_0\,t}\,\sin(\sqrt{1 - \zeta^2}\,\omega_0\,t + \phi_{\text{hom}}) \tag{A.2}$$

where A and ϕ depend on the boundary conditions. The homogeneous solution will eventually be damped out depending on the damping ratio ζ, so after an adequate time, the trajectory will be described by just the inhomogeneous solution.

In opto-mechanics, the quality factor Q is of main interest. It is defined as

$$Q = \frac{1}{2\,\zeta} = \frac{1}{2}\,T_{1/\mathrm{e}}\,\omega_0 \tag{A.3}$$

where $T_{1/\mathrm{e}}$ denotes the time after which the system's amplitude has dropped to $\frac{1}{\mathrm{e}}$ of its original value. This corresponds to $\frac{1}{2}$ times the number of oscillations the system does within the time $T_{1/\mathrm{e}}$. Since damping ratios add as $\zeta_{\text{total}} = \zeta_1 + \ldots + \zeta_n$, quality factors add as

$$\frac{1}{Q_{\text{total}}} = \frac{1}{Q_1} + \ldots + \frac{1}{Q_n} \tag{A.4}$$

The solution to the inhomogeneous equation can be obtained by continuous Fourier transformation $\mathcal{F}$ of (A.1):

$$-\omega_{\mathcal{F}}^2 \, \mathcal{F}(x)(\omega_{\mathcal{F}}) + 2\mathrm{i}\,\xi\,\omega_0\,\omega_{\mathcal{F}}\,\mathcal{F}(x)(\omega_{\mathcal{F}}) + \omega_0^2\,\mathcal{F}(x)(\omega_{\mathcal{F}}) = \frac{\mathcal{F}(F_{\text{ext}})(\omega_{\mathcal{F}})}{m}$$

$$\Leftrightarrow \quad x(t) = \mathcal{F}^{-1}\left(\frac{\mathcal{F}(F_{\text{ext}})(\omega_{\mathcal{F}})}{m\left(-\omega_{\mathcal{F}}^2 + 2\mathrm{i}\,\zeta\,\omega_0\,\omega_{\mathcal{F}} + \omega_0^2\right)}\right)(t). \qquad (A.5)$$

A.1. Driving with white noise

If the driving is white noise, the Fourier transform of the driving force is unity (this is the definition of white noise); $\mathcal{F}(F_{\text{ext}}) = F_0\,1$. With (A.5) we get

$$|\mathcal{F}(x)(\omega_{\mathcal{F}})|^2 = \frac{(F_0/m)^2}{\left(\omega_0^2 - \omega_{\mathcal{F}}^2\right)^2 + \left(2\,\zeta\,\omega_0\,\omega_{\mathcal{F}}\right)^2}.$$

A.2. Harmonic driving

For a periodic harmonic driving force $F_{\text{ext}}(t) = F_0\,\sin(\omega\,t)$,

$$\mathcal{F}(F_{\text{ext}})(\omega_{\mathcal{F}}) = \frac{\sqrt{2\pi}}{2\mathrm{i}}\,F_0\,\left(\delta(\omega_{\mathcal{F}} - \omega) - \delta(\omega_{\mathcal{F}} + \omega)\right)$$

which inserted into (A.5) leads to the solution for the inhomogeneous equation

$$x_{\text{inhom}}(t) = \frac{F_0}{m\,Z}\,\sin(\omega\,t + \phi_{\text{inhom}}) \quad \text{with} \quad \begin{aligned} Z &= \sqrt{(\omega_0^2 - \omega^2)^2 + (2\,\omega_0\,\omega\,\zeta)^2} \\ \phi_{\text{inhom}} &= \arctan\left(\frac{-2\,\omega_0\,\omega\,\zeta}{\omega_0^2 - \omega^2}\right) \end{aligned}.$$

$$(A.6)$$

A.3. Lock-in amplification

To obtain the unknown parameters in (A.6), lock-in amplification provides a nice way of extracting the amplitude $\frac{F_0}{m\,Z}$. This is done by driving the system with a certain frequency ω_{lock} and integrating the product of the reference signal and the response signal $I(t)$:

$$I_{\text{lock}}(\omega_{\text{lock}}) = \frac{1}{T}\int_0^T \sin\left(\omega_{\text{lock}}t' + \phi_{\text{lock}}\right)\,I(t')\,\mathrm{d}t'$$

Insertion of (A.6) for the response signal with driving frequency ω_{lock} yields

$$
\begin{aligned}
I_{\text{lock}}(\omega_{\text{lock}}) = & \frac{1}{2} \frac{F_0/m}{Z(\omega_{\text{lock}})} \cos(\phi_{\text{lock}} - \phi_{\text{inhom}}) \\
& - \frac{1}{2\,T} \frac{F_0/m}{Z(\omega_{\text{lock}})\,\omega_{\text{lock}}} \left[\sin(2\,\omega_{\text{lock}}\,T + \phi_{\text{lock}} + \phi_{\text{inhom}}) \right. \\
& \left. - \sin(\phi_{\text{lock}} + \phi_{\text{inhom}}) \right].
\end{aligned}
$$

For sufficiently large integration times T, the second term will approach zero and one gets the amplitude of the driven oscillator, $\frac{F_0/m}{Z(\omega_{\text{lock}})}$ and the phase ϕ_{inhom} (since ϕ_{lock} is known).

A.4. Approximation

Both the squared total amplitude of the Fourier transformed amplitude of the white noise driven oscillator and the squared amplitude of the periodically driven oscillator are *relativistic Breit–Wigner distributions* of the form

$$
f(\omega) = \frac{(F_0/m)^2}{\left(\omega_0^2 - \omega^2\right)^2 + \left(2\,\zeta\,\omega_0\,\omega\right)^2}.
$$

When the quality factor Q is large, the *Cauchy–Lorentz* distribution is a very good approximation. It is written as

$$
D_{CL}(\omega) = \left(\frac{F_0/m}{2\,\omega_0^2\,\zeta} \right)^2 \frac{(\zeta\,\omega_0)^2}{(\omega - \omega_0)^2 + (\zeta\,\omega_0)^2}. \tag{A.7}
$$

Both distributions are compared in figure A.1.
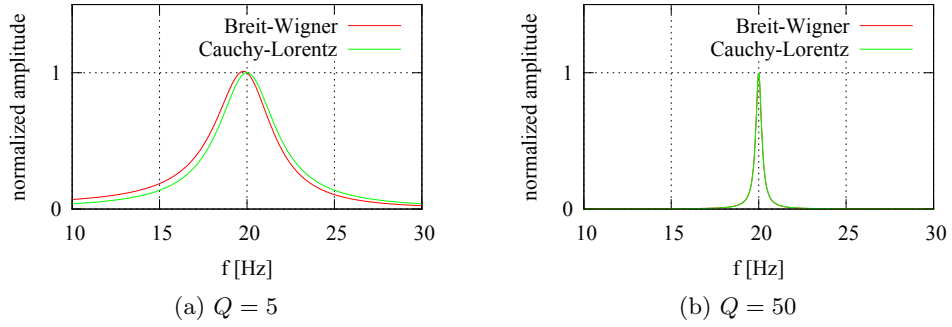
(a) $Q = 5$　　　　　　　　　　　　　(b) $Q = 50$

Figure A.1.: Comparison of the relativistic Breit-Wigner peak and the Cauchy-Lorentz approximation for a frequency of 20 Hz.

B. Technical notes

In this section we cover some auxiliary calculations and technical remarks concerning the experimental setup.

B.1. Q and mechanical heating

The effective occupation number n_{eff} of a laser-cooled oscillator under certain restrictions is given by [30]

$$n_{\text{eff}} = \frac{\Gamma_{\text{heating}} + A_+}{\gamma_m + \Gamma_{\text{laser}}},$$

where Γ_{heating} is the heating rate through coupling to a thermal bath, $\gamma_m = \frac{\omega}{Q}$ is the natural coupling rate, $\Gamma_{\text{laser}} = A_- - A_+$ is the laser cooling rate and A_+, A_- are the rates at which laser photons are scattered into the Stokes/anti-Stokes sideband of the oscillator.

We ask for the rate Γ_{heating} at which a system at an occupation number n_{eff} relaxes to equilibrium with its environment (approaching the equilibrium occupation $\bar{n}$) if no cooling is applied. This process can be approximated by

$$n(t) = \bar{n} - (\bar{n} - n_{\text{eff}})\,\mathrm{e}^{-\gamma_m t}.$$

From the definition of Γ_{heating},

$$\Gamma_{\text{heating}} := \dot{n}(t = 0) = \gamma_m\,\bar{n} - \gamma_m\,n_{\text{eff}}$$

which approaches

$$\Gamma_{\text{heating}} \approx \gamma_m\,\bar{n} \tag{B.1}$$

if the bath temperature is high; $\bar{n} \gg n_{\text{eff}}$. From Bose-Einstein statistics, the thermal occupation number is given by

$$\bar{n} = \left(\mathrm{e}^{\frac{\hbar\omega}{k_B T}} - 1\right)^{-1} \approx \frac{k_B T}{\hbar\omega} \quad \text{for} \quad \hbar\omega \ll k_B T,$$

where the condition is fulfilled if the bath temperature is high compared to the ground state temperature. Inserting this into (B.1) and using $\gamma_m = \frac{\omega}{Q}$, we get

$$\Gamma_{\text{heating}} \approx \frac{k_B\,T}{\hbar\,Q}$$

which does *not* depend on ω. This is the reason why systems with very high quality factors are interesting, even if they have very low frequencies.

B.2. Laplace of B and B^2

The static Maxwell equations without currents yield

$$\nabla \cdot \boldsymbol{B} = 0 \quad \text{and} \quad \nabla \times \boldsymbol{B} = 0.$$

Therefore $\boldsymbol{B}$ and its individual components B_1, B_2, B_3 fulfill Laplace's equation:

$$\nabla^2 \boldsymbol{B} = \nabla(\nabla\boldsymbol{B}) - \nabla \times (\nabla \times \boldsymbol{B}) = 0. \tag{B.2}$$

Furthermore [21],

$$\begin{aligned}
\nabla^2 \boldsymbol{B}^2 =& (\partial_1^2 + \partial_2^2 + \partial_3^3)\,(B_1^2 + B_2^2 + B_3^2)\\
=& 2\,(\partial_1 B_1)^2 + 2\,(\partial_2 B_1)^2 + \ldots + 2\,(\partial_3 B_3)^2\\
& + 2\,B_1 \partial_1^2 B_1 + 2\,B_1 \partial_2^2 B_1 + \ldots + 2\,B_3 \partial_3^2 B_3\\
=& 2\,(\nabla B_1)^2 + 2\,(\nabla B_2)^2 + 2\,(\nabla B_3)^2\\
& + 2\,B_1 \nabla^2 B_1 + 2\,B_2 \nabla^2 B_2 + 2\,B_3 \nabla^2 B_3\\
\overset{(B.2)}{=}& 2\,(\nabla B_1)^2 + 2\,(\nabla B_2)^2 + 2\,(\nabla B_3)^2 \geq 0
\end{aligned}$$

B.3. Excluding sources of peak broadening

To check if the driving of the piezo is smeared out at low frequencies, which would set a lower bound on the achievable width of the peaks measured when performing lock-in scans, we independently checked the output of the lock-in-amplifier (figure B.1a) and of the piezo by driving it with a frequency generator and performing the usual reflection measurement, but without the magnets (figure B.1b). Both frequencies were set to 15 Hz. For the output of the lock-in amplifier, we obtained $\omega = 14.9998[2]$ Hz with $Q = 12.9[43] \cdot 10^3$. The output of the frequency generator was $\omega = 15.0[3]$ Hz with $Q = 90.8[52] \cdot 10^3$. Therefore, device limitations are not an issue.

(a) Sharpness of the frequency output of the lock-in amplifier.

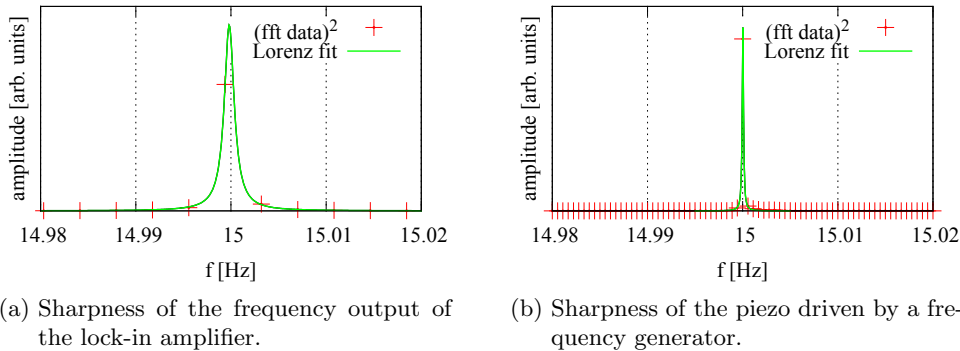(b) Sharpness of the piezo driven by a frequency generator.

Figure B.1.: Sharpness of the device signals used throughout the experiments. The peaks are significantly narrower than those seen in the measurements with the sample.

B.4. Interferometric readout of noisy low-f systems

This section should serve as an overview of the obstacles we encountered when setting up the experimental setup and as an advice which mistakes one should avoid when dealing with low-frequency oscillators in interferometers.

B.4.1. Why we used a low-frequency vibration isolation stage and why we should have bought a bigger one

In the first version of the setup, all components including the chamber were mounted on a standard optical table. When performing interferometric measurements in this setup, it turned out that the oscillations from low-frequency noise of the lab, which made their way through the optical table to the sample, had an amplitude of more than one or even two times a wavelength (1064 nm). The directly detectable displacement range of a Michelson interferometer is limited to half a wavelength and displacements of more than that will show up as $\sin(\sin(t))$ type modulations, leading to higher orders in the spectrum.

Our initial approach to this problem was to put the vacuum chamber on a special vibration isolation table for low frequencies. We chose a model from *minus k* with a maximum payload of 14 kg and an area of about $30 \times 30\,\text{cm}^2$ which was sufficient for mounting the chamber. When performing the first interferometric measurements with the now vibration-isolated chamber and the optical components still directly mounted on the optical table, a huge noise at low frequencies became evident, suppressing all other peaks which were visible before (figure B.2). This massive noise is simply explained by the fact that the sample mirror was damped in low frequen-

cies, while all other components in the setup were still vibrating in this frequency range. Therefore the interferometer collected everything the table dampened out. The solution for this problem was to mount *all* optical components on the vibration isolation stage.
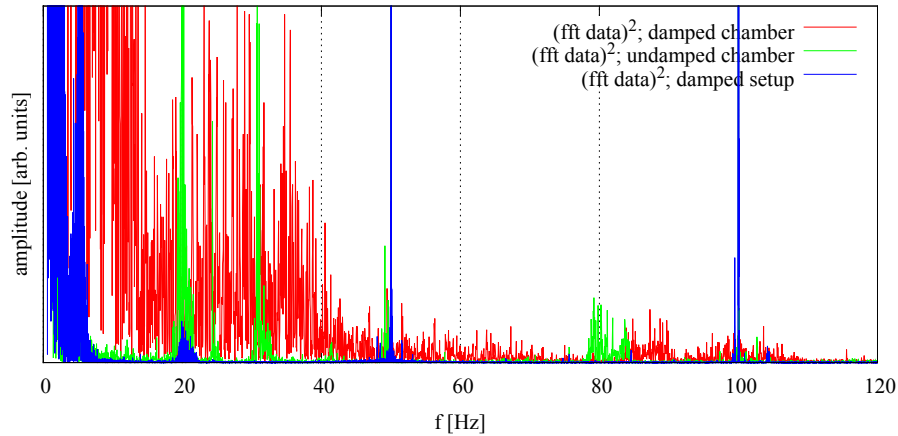

Figure B.2.: Comparison of fourier noise spectra of the undamped setup, the setup with the vibration-isolated vacuum chamber and the setup with all components isolated.

Mounting a whole interferometer on the stage which originally was planed for just the vacuum chamber, while at the same time keeping the center of mass in the middle of the stage and the total payload below the max of 14 kg was a task which could only be accomplished with a vertical interferometer as seen in figure 3.3b, page 11. Eventually it lead to less noisy spectra (figure B.2). With the chamber, some new peaks at 150 Hz, 310 Hz, 410 Hz, 510 Hz, 610 Hz showed up which could not be seen before - probably they are mechanical modes of the vibration isolation stage. With the combined damping from both tables, the undriven motion of the sample was decreased, but the amplitude was still more than a half wavelength. Therefore, higher orders in the interferometric measurements could never be totally eliminated.

The biggest problem with the interferometric readout scheme is that it is not compatible with driving in this setup. Every driven frequency was directly visible as a sharp peak in the spectrum as shown in figure B.3. This makes it impossible to identify mechanical peaks by checking their response to external driving.
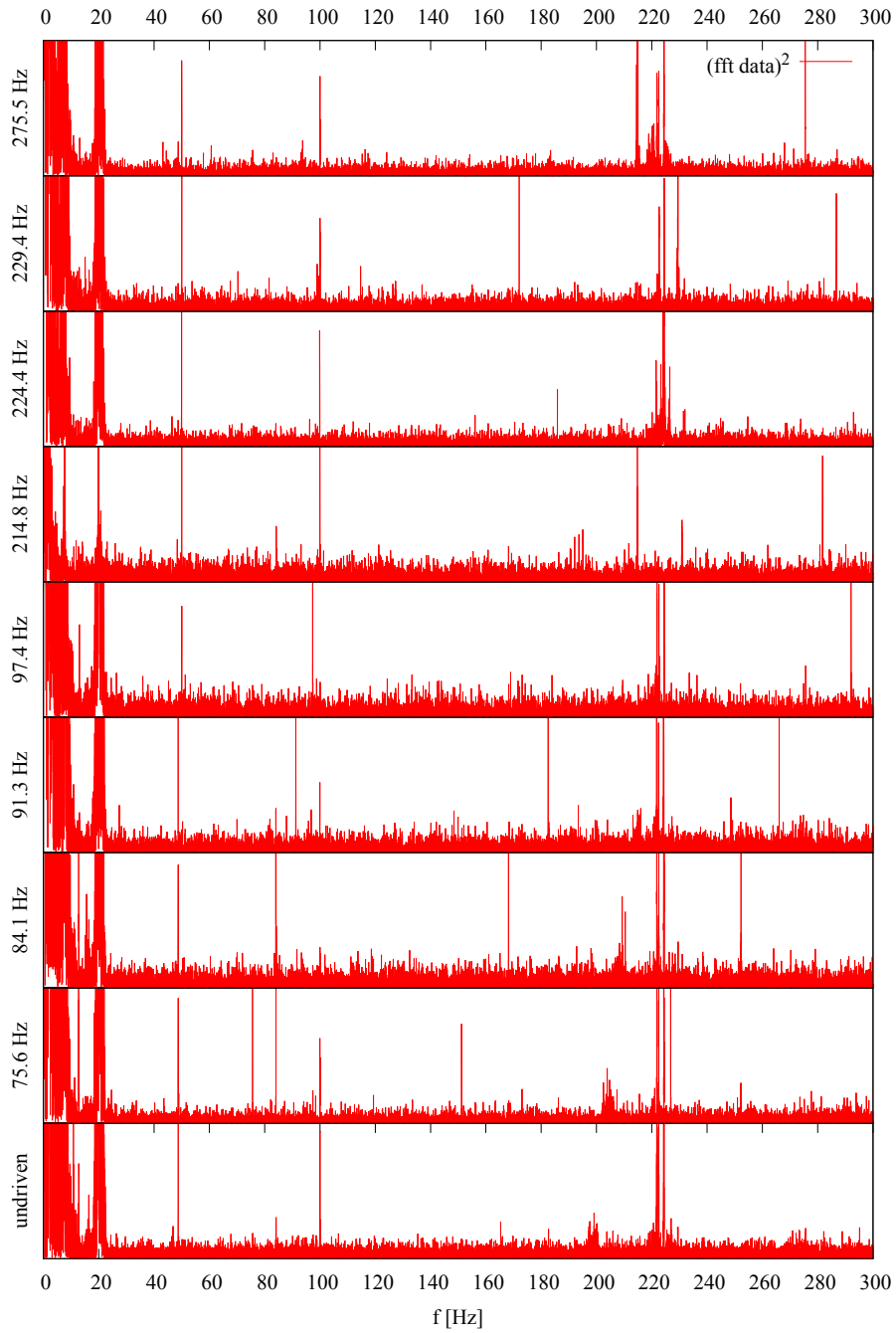
Figure B.3.: Interferometric spectra with certain frequencies driven (left column). Every driven frequency shows up as a sharp peak in the spectrum.

B.4.2. Why we built a HV chamber and why we should have built an UHV chamber

With all optical components on the low-frequency vibration isolation stage, nice results could be achieved as long as there was no connection from the setup to anything else in the lab, e.g. a pump. Connecting a pump completely canceled the effect of the stage and lead to massive noise with sidebands and many multiple-frequency peaks becoming visible (figure B.4).
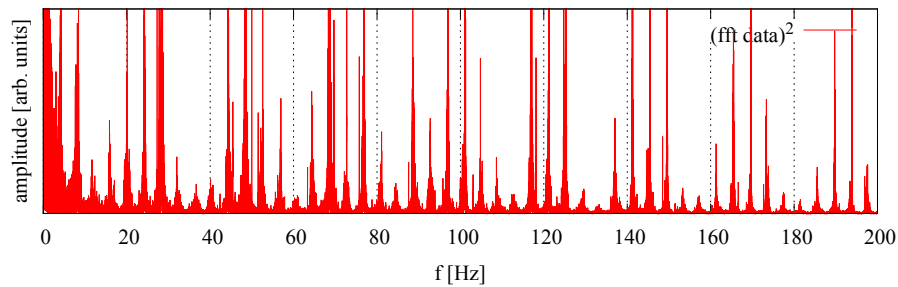
Figure B.4.: Interferometric spectrum at low vacuum with the pump running.

Our idea to solve this issue was to have a connection from the vacuum chamber to a fixed block mounted to the optical table (visible in figure 3.3b, page 11) with some low-frequency absorbing bellows and another connection from there to the pump with high-frequency absorbing bellows to effectively filter the pump using the weight of the optical table. Sadly, this did not work at all and produced the same amount of noise as seen with a direct connection between pump and chamber. However, it turned out to be quite easy to break the vibration isolation stage with this configuration. Since the bellows contract when evacuated and the stage has to be clamped down during that process,[1] it was almost impossible to adjust the bellow suspension on the optical table in order such that it did not exert a force on the stage. A few adjustment tries eventually lead to a broken spring, which we did not notice until all measurements were finished.

From this observations it seems reasonable to completely detach the chamber from the pump while interferometric measurements are performed. However, the pressure of our HV setup goes up quite fast while no pump is connected - we could not hold 10^{-3} mbar for more than a few minutes, which made the measurements described in section 4.1 quite stressful. It would have been a good idea to build the whole setup with UHV components in order to be able to hold low pressures longer, since holding a pressure of 10^{-5} mbar is no problem with a UHV chamber. Another solution would

---

[1] From the specifications of the stage manufacturer, it is not allowed to even touch the payload when the stage is *set free* due to the fragile springs which might break.

have been to design the HV chamber in a way that an ion pump, which does not have mechanical elements, can be mounted, allowing continuous pumping of the chamber.

B.4.3. Why dealing with low frequency non-rigidly suspended oscillators is painful

Apart from the noise problem described above, there are further issues with a levitating low-frequency system like this.

Because of the low frequencies, a usual scheme to find mechanical modes and frequencies, which is connecting a frequency spectrum analyzer to the output and scanning through driving frequencies in order to see a response, is difficult for two reasons: First, peaks with similar frequencies (small spacing) broaden into one and second, the resolution is limited by the refreshing rate - when the screen is refreshed every 2 seconds, the resolution limit is $0.5\,\text{Hz}$.[2]

In free-space, it is necessary to hit the sample in a way the beam is reflected into itself. One could solve this problem in a fiber interferometer, but there one would have to map the surface of the sample in x_1 and x_2 direction in order to find all modes (since beam displacement cannot directly be seen).

The adjusted setup was so sensitive, that placing laser safety goggles (or any other object of similar or higher weight) anywhere on the optical table caused the beam to almost go out of the range of the quadrant diode. In a busy lab with several people working on other experiments, it was actually quite a challenge to not touch anything slightly attached to the table for the whole time a measurement ran - which was between 5 minutes and a few hours. Therefore, for further experiments more care should be taken to exclude sources of noise and increase the repeatability, e.g. heavier vibration isolation systems, more stable mounts for optics and avoidance of *vertical* beam paths if possible.

Ultimately, even the worst and most painful experiment is no excuse for being stupid, as was obvious when some of the magnets, which were still needed for the experiment, accidentally were used for the creation of a PhD celebration hat.

---

[2]The latter issue is a general problem which can also occur for high-frequency mechanics with very high quality, since the resolution of the frequency spectrum needs to match the peak width given by $\gamma = \frac{\omega_0}{2Q}$.

Bibliography

[1] M Aspelmeyer and K Schwab. Focus on mechanical systems at the quantum limit. *New Journal of Physics*, 10(9):95001, 2008.

[2] T J Kippenberg and K J Vahala. Cavity optomechanics: back-action at the mesoscale. *Science*, 321(5893):1172–6, August 2008.

[3] M Arndt, M Aspelmeyer, and A Zeilinger. How to extend quantum experiments. *Fortschritte Der Physik*, 57(11-12):1–10, 2009.

[4] C Genes, A Mari, D Vitali, and P Tombesi. Quantum effects in optomechanical systems. *Advances In Atomic, Molecular, and Optical Physics*, 57(December):33–86, 2009.

[5] E Schrödinger. Die gegenwärtige Situation in der Quantenmechanik. *Die Naturwissenschaften*, 23(49):807–812, 1935.

[6] F Marquardt, J Chen, A Clerk, and S Girvin. Quantum Theory of Cavity-Assisted Sideband Cooling of Mechanical Motion. *Physical Review Letters*, 99(9), August 2007.

[7] J Dobrindt, I Wilson-Rae, and T Kippenberg. Parametric Normal-Mode Splitting in Cavity Optomechanics. *Physical Review Letters*, 101(26), December 2008.

[8] Simon Gröblacher, Jared B. Hertzberg, Michael R. Vanner, Garrett D. Cole, Sylvain Gigan, K. C. Schwab, and Markus Aspelmeyer. Demonstration of an ultracold micro-optomechanical oscillator in a cryogenic cavity. *Nature Physics*, 5(7):485–488, June 2009.

[9] D E Chang, C A Regal, S B Papp, D J Wilson, J Ye, O Painter, H J Kimble, and P Zoller. Cavity opto-mechanics using an optically levitated nanosphere. *Proceedings of the National Academy of Sciences of the United States of America*, 107(3):1005–10, January 2010.

[10] P F Barker. Cavity cooling of an optically trapped nanoparticle. *Physical Review A*, 81(2), February 2010.

[11] O Romero-Isart, A Pflanzer, M Juan, R Quidant, N Kiesel, M Aspelmeyer, and J Cirac. Optically levitating dielectrics in the quantum regime: Theory and protocols. *Physical Review A*, 83(1), January 2011.

[12] S Singh, G Phelps, D Goldbaum, E Wright, and P Meystre. All-Optical Optomechanics: An Optical Spring Mirror. *Physical Review Letters*, 105(21), November 2010.

[13] U Leonhardt and T G Philbin. Quantum levitation by left-handed metamaterials. *New Journal of Physics*, 9(8):254–254, August 2007.

[14] D Garmire, H Choo, R Kant, S Govindjee, C H Sequin, R S Muller, and J Demmel. *Diamagnetically Levitated MEMS Accelerometers*. IEEE, 2007.

[15] T Matsushita. *Flux Pinning in Superconductors*. Springer, 2006.

[16] S Earnshaw. On the nature of the molecular forces which regulate the constitution of the luminiferous ether. *Trans. Camb. Phil. Soc*, 7:97 – 112, 1842.

[17] J R Reitz, F J Milford, and R W Christy. *Foundations of Electromagnetic Theory (4th Edition)*. Addison Wesley, 2008.

[18] E W Hones and W G Hones. Magnetic levitation device and method, February 1994.

[19] M D Simon. Spin stabilized magnetic levitation. *American Journal of Physics*, 65(4):286, 1997.

[20] M D Simon and A K Geim. Diamagnetic levitation: Flying frogs and floating magnets (invited). *Journal of Applied Physics*, 87(9):6200, 2000.

[21] M V Berry and A K Geim. Of flying frogs and levitrons. *European Journal of Physics*, 18(4):307–313, July 1997.

[22] A. K. Geim, M. D. Simon, M. I. Boamfa, and L. O. Heflinger. Magnet levitation at your fingertips. *Nature*, 400(6742):323–324, July 1999.

[23] M D Simon, L O Heflinger, and A K Geim. Diamagnetically stabilized magnet levitation. *American Journal of Physics*, 69(6):702–713, 2001.

[24] O Romero-Isart. Private conversation, 2011.

[25] D Patrick and T Beebe. On the origin of large-scale periodicities observed during scanning tunneling microscopy studies of highly ordered pyrolytic graphite. *Surface Science*, 297(3):L119–L121, December 1993.

[26] M McCaig and A G Clegg. *Permanent Magnets in Theory and Practice.* John Wiley & Sons Inc, 1987.

[27] R Engel-Herbert and T Hesjedal. Calculation of the magnetic stray field of a uniaxial magnetic domain. *Journal of Applied Physics*, 97(7):074504, 2005.

[28] H Sumali and T G Carne. Air-Drag Damping on Micro-Cantilever Beams. *sem-proceedings.com*, 2004.

[29] L Kapjin and P Kyihwan. Modeling eddy currents with boundary conditions by using Coulomb's law and the method of images. *IEEE Transactions on Magnetics*, 38(2):1333–1340, March 2002.

[30] C Genes, D Vitali, P Tombesi, S Gigan, and M Aspelmeyer. Ground-state cooling of a micromechanical oscillator: Comparing cold damping and cavity-assisted cooling schemes. *Physical Review A*, 77(3), March 2008.

List of Tables

List of Figures

Curriculum Vitae

Quantum Optics, Quantum Nanophysics, Quantum Information
Boltzmanngasse 5
1090 Vienna, Austria

Jonas Schmöle

BSc

☏ *+43 (0)681 20232868*
☎ *+43 (0)1 4277 72533*
✉ *jonas.schmoele@univie.ac.at*

━━━━━━━━ Research experience

2010–2011 **Master thesis:** ***"Magnetic levitation in optomechanics"***, *Quantum Optics, Quantum Nanophysics, Quantum Information,* University of Vienna.
Mentored by Markus Aspelmeyer

2010 **Research assistant in experimental quantum computation**, *Quantum Optics, Quantum Nanophysics, Quantum Information,* University of Vienna.
Worked on automated quantum tomography; mentored by Philip Walther

2009 **Research in geometric phases**, *Department of Quantum Information,* Uppsala University.
Worked on geometric phases through displacement and squeezing; mentored by Erik Sjöqvist and Marie Ericsson

2009 **Bachelor thesis:** ***"Precession effects in surroundings of slowly rotating masses"***, *Max-Planck institute for dynamics and self-organization,* Göttingen, *grade 1.0 (A).*
Mentored by Folkert Müller-Hoissen

2008 **Project Laboratory:** ***"Very low cost quantum cryptography"***, *Faculty of Physics,* Georg-August University Göttingen.
Mentored by Thomas Kurz

<div style="float:left">▬▬▬▬</div> Education

2010–2011 **Master of Science in Physics**, *Faculty of Physics*, University of Vienna.

2009–2010 **Studies in physics and mathematics**, *Ångströmlaboratoriet*, Uppsala Universitet.

2006–2009 **Bachelor of Science in Physics**, *Faculty of Physics*, Georg-August University Göttingen, *grade 1.5 (A-) with distinction*.

2003–2006 **Abitur**, *Albert-Schweitzer Gymnasium*, Kassel, *grade 1.3 (A-)*.
- Major in physics and mathematics.
- Honored by the Deutsche Physikalische Gesellschaft (German Society for Physics) for the best Abitur with a major in physics.
- Honored by the school with the medal of honor for outstanding achievements in an extracurricular competition.

<div style="float:left">▬▬▬▬</div> Awards

2011 *"Merck-Förderpreis für ehemalige Jungforscher"* ("Merck fellowship award for former young scientists")

2010 *"Leistungsstipendien der Universität Wien"* (academic achievement scholarship from the university of Vienna)

2006 National champion (highest level) of the *Jugend forscht* scientific youth competition with *"Quantenmechanische Experimente mit einzelnen Photonen"* (*"Quantum mechanical experiments with single photons"*)

<div style="float:left">▬▬▬▬</div> Independent activities

2008 Co-founder of *Förderverein SchülerForschungsZentrum Nordhessen (StudentScienceCenter northern hesse support associaton)*

2007, 2008 Internship at *GSI Helmholtz Center for Heavy Ion Research* in Darmstadt, Germany

2006-2009 Mentoring of teenagers in natural science projects at *Physik-Club Kassel (PhysicsClub Kassel)* and *SchülerForschungsZentrum Nordhessen*

2002–2006 Participation in *PhysikClub Kassel* with projects in chaos physics, special relativity, network theory and quantum mechanics

Languages

German	**Native speaker**	
English	**Fluent**	
French	**Basic knowledge**	*Educted in school for five years*
Swedish	**Basic knowledge**	*Educated in university (one term); studies in Sweden (one term)*

Computer skills

Operating systems	Windows (good), Linux (basics)	Programming	Labview, Mathematica (good), Java, C, Delphi (basics)
Office, typesetting	MS Office, OpenOffice, LaTeX, BibTex (good)	Graphics	Photoshop (advanced), InkScape, Illustrator (good), Gimp (basics)
Simulation, CAD	Comsol Multiphysics, SolidWorks (basics)		

Leisure activities

Artistic	Photography, digital image creation and processing, music (playing the guitar and digital creation), painting
Sports	Cycling, working out, running, swimming, squash, basketball